

# Large-Dimensional Multibody Dynamics Simulation Using Contact Nodalization and Diagonalization

Jeongmin Lee, Minji Lee, and Dongjun Lee

**Abstract**—We propose a novel multibody dynamics simulation framework that can efficiently deal with large-dimensionality and complementarity multi-contact conditions. Typical contact simulation approaches perform contact impulse-level fixed-point iteration (IL-FPI), which has high time-complexity from large-size matrix inversion and multiplication, as well as susceptibility to ill-conditioned contact situations. To circumvent this, we propose a novel framework based on velocity-level fixed-point iteration (VL-FPI), which, by utilizing a certain surrogate dynamics and contact nodalization (with virtual nodes), can achieve not only inter-contact decoupling but also their inter-axes decoupling (i.e., contact diagonalization). This then enables us to one-shot/parallel-solve the contact problem during each VL-FPI iteration-loop, while the surrogate dynamics structure allows us to circumvent large-size/dense matrix inversion/multiplication, thereby, significantly speeding up the simulation time with improved convergence property. We theoretically show that the solution of our framework is consistent with that of the original problem and, further, elucidate mathematical conditions for the convergence of our proposed solver. Performance and properties of our proposed simulation framework are also demonstrated and experimentally-validated for various large-dimensional/multi-contact scenarios including deformable objects.

## I. INTRODUCTION

AS technology and automation advance, robots performing diverse tasks in various environments on behalf of humans are becoming an increasingly essential topic [1]. Robots no longer do specific tasks in a stationary and well-known environment, necessitating the ability to notice changes in their surroundings and react immediately through interaction. In this regard, enhancing online performance and flexibility by offline pre-training has recently emerged as a very promising solution. These concepts have been implemented in a variety of ways (e.g., self-supervised learning [2], [3], reinforcement learning [4], [5]) and have been used to succeed in tasks in a variety of challenging situations (e.g., climbing in complex terrain [6], tight tolerance assembly [7]).

Since the approaches described above can be broadly understood in terms of optimization, they commonly require large amounts of high-quality ‘data’ to achieve adequate performance and robustness. These data can also be gathered in real-world contexts, but by using virtual environments (i.e., simulation), the data collecting process becomes considerably

safer and faster, and the environment can be adjusted without the need for human intervention. Furthermore, perfect knowledge of the system can be used for more efficient learning [8], [9] and does not necessitate a separate estimating approach to collect data. As a result, simulation is frequently utilized as a backbone to train robots to do challenging tasks (i.e., sim-to-real transfer [10]–[12]).

However, for efficient data collection, simulation must be both fast and accurate. One of the most important yet challenging issues in dynamic simulation of robot applications is contact [13], as it inevitably occurs in situations where the robot interacts with the environment and other objects, and have instantaneous and complementary properties. Contact simulation can be typically written in the following form of discrete-time dynamics equation:

$$A_k \hat{v}_k = b_k + J_{c,k}^T \lambda_{c,k} \quad (1)$$

where  $A_k \in \mathbb{R}^{n \times n}$ ,  $b_k \in \mathbb{R}^n$  are constructed from the system dynamics at the  $k$ -th time step,  $\hat{v}_k \in \mathbb{R}^n$  is the representative velocity of the time step,  $J_{c,k} \in \mathbb{R}^{3n_c \times n}$  is the contact Jacobian,  $\lambda_{c,k} \in \mathbb{R}^{3n_c}$  is the contact impulse,  $n$  is the system dimension, and  $n_c$  is the contact number at the time step. To solve this dynamics equation (1),  $\hat{v}_k$  and  $\lambda_{c,k}$  that satisfy the Signorini-Coulomb condition (SCC, see Sec. II-B for detail) as well as (1) must be obtained.

SCC is mainly based on non-linear complementarity relation between  $J_{c,k} \hat{v}_k$  and  $\lambda_{c,k}$ . In typical robotic simulation, solving contacts begins with the transformation of (1) to contact impulse space s.t.,

$$J_{c,k} \hat{v}_k = J_{c,k} A_k^{-1} J_{c,k}^T \lambda_{c,k} + J_{c,k} A_k^{-1} b_k \quad (2)$$

where  $J_{c,k} A_k^{-1} J_{c,k}^T$  is called Delassus operator [14]. This impulse-based formulation (2) implies the linear relation between contact impulse and the velocity relative to the contact frame. Based on this formulation, various algorithms [15]–[18] have been proposed to find a proper collision response that satisfies the contact conditions. Although these algorithms are different from each other, they have a common structure of performing impulse-level fixed point iteration (IL-FPI) while locally solving each contact. However, IL-FPI based methods typically suffer from the following challenges:

- Structure of the matrix  $A_k$  in (1) is dense and time-varying due to numerous couplings between states, which makes the computation of Delassus operator in (2) intractable especially for a large-size dynamics with varying contact points.
- In the case of ill-conditioned contact situations (i.e., the condition number of the Delassus operator is poor), the

This research was supported by the Industrial Strategic Technology Development Program (20001045) of the Ministry of Trade, Industry & Energy (MOTIE) of Korea; and the Engineering Research Center Program for Soft Robotics (2016R1A5A1938472) of the National Research Foundation (NRF) funded by the Ministry of Science, ICT & Future Planning (MSIP) of Korea.

The authors are with the Department of Mechanical & Aerospace Engineering and IAMD, Seoul National University, Seoul, Republic of Korea. {ljmlgh,mingg8,djlee}@snu.ac.kr. Corresponding author: Dongjun Lee.

IL-FPI adopted to (2) converges slowly and often fails, resulting in implausible behavior of the simulation.

For the above reasons, it is hard to efficiently simulate a high degree of freedom (DOF) systems where multiple contacts occur, especially scenarios involving deformable objects.

IL-FPI based approaches [15]–[18] may be characterized as executing fixed-point iteration to meet contact complementarity condition while intrinsically reflecting (1). In contrast, in this paper, we present a new method that uses fixed-point iteration to satisfy (1) while keeping the contact condition (i.e., SCC). To implement this concept, we devise a velocity-level fixed-point iteration (VL-FPI) that generates a surrogate dynamics and solve contact problem with respect to the surrogate dynamics at each iteration loop. We then propose the idea of contact nodalization, which turns all contacts into nodal situations (i.e., contact with Cartesian nodal points) while precisely preserving the contact condition. On this basis, we can conduct contact diagonalization on each contact problem of surrogate dynamics and solve it in a single step. The main features of our framework can be summarized as follow:

- *Scalable*: Entire procedure of the solver consists solely of matrix-vector multiplication and simple algebraic operations, resulting low time and memory complexity.
- *Accurate*: Dynamics and contact conditions are precisely enforced, resulting accurate contact simulation as demonstrated by experimental validations.
- *Convergent*: Convergence are theoretically investigated and practically proved to have fast and robust convergence even for ill-conditioned problems.
- *Versatile*: Diverse formulations including a combination of rigid-deformable body, maximal-generalized coordinate can be dealt with. Furthermore, it is compatible with various integrator types and friction models as well.

From now on, we refer to the framework as simulation using contact nodalization and diagonalization (COND). We also release an implementation of COND for specific scenario (cable winding manipulation, see Sec. V for detail) so that it can be utilized for simulation and learning benchmarks: [https://github.com/INRoL/inrol\\_sim\\_cablewinding](https://github.com/INRoL/inrol_sim_cablewinding).

The problem of solving dynamics with contact has been studied for a long time. By linearizing the friction cone as a polygonal shape, non-linear complementarity problem (NCP) nature of the contact dynamics is reduced to linear complementarity problem (LCP) [19] and can be solved using direct pivoting method [20]. While the problem can be exactly solved, it suffers from high time-complexity of impulse space conversion and solving process. Also, due to linearized friction cone, unphysical frictional behavior can be generated [14].

Numerous iterative methods have been proposed to overcome this limitation. One of the most prevalent methods is projected Gauss-Seidel (PGS) method [14], which solves (2) using Gauss-Seidel type IL-FPI while projecting the solution to the friction cone. As the method is faster than direct method and can handle with diverse contact formulation (e.g., NCP, LCP, cone complementarity problem (CCP [21]), and convex [22]), it has been adopted widely in many open source simulation softwares (e.g., Bullet [23], MuJoCo [24]). The projection step

are also sometimes replaced with a slight modification using the bisection [15] and Newton [16] methods for efficiency in specific situations. However as previously mentioned, these methods are still not scalable due to their reliance on the impulse space conversion and can converge slowly for the ill-conditioned contact situations.

To avoid the scalability issue of large size contact problems, model order reduction is utilized to reduce the system dimension in [25], [26] with open-source framework SOFA [27]. However, they assume small deformation or limited modes of system behavior, thus, the applicable scenarios are restricted. Methods of locally and iteratively dealing with each of the constraints present in large size dynamics are widely used in the graphics area [28], [29]. The main limitation here is that those techniques generate contact behavior based on constraint potential rather than SCC, therefore, their behavior is often not physically correct as described in [30]. Also, local and iterative constraint resolving approaches are incompatible with generalized coordinates representation which is widely used in robotic simulation.

Recently, several methods to deal with the large size dynamics with complementarity contact have been proposed. In [31], PGS is transformed for subsystem-based parallel architecture, but the method is limited to systems with few interconnections between subsystems. In [30] and [32], efficient solvers that can simulate objects such as clothes and hair are proposed while avoiding impulse space conversion. In contrast to our framework, they still rely on the global relaxation/linear solving process and cannot deal with general rigid body representation. Another notable work is [33] that develops a non-smooth Newton method to solve contact conditions using Schur-complement and complementarity preconditioner. Yet, multiple large-size linear solving processes are required for each time step and the system depends to lumped mass representation.

The rest of the paper is organized as follows. Sec. II will explain how to create constrained dynamics with contact in a discrete-time domain (i.e., (1)). Then in Sec. III, our main algorithm of dynamics solver in COND will be described in detail. Sec. IV will investigate the convergence of the solver. The simulation and experiment result to validate the performance of COND will be presented in Sec. V. Finally, conclusions and some future work will be discussed in Sec. VI.

## II. CONSTRAINED DYNAMICS WITH CONTACT

In this section, we will describe how we construct the dynamic equation with multiple constraints and contact.

### A. Dynamics Integration

We formulate discrete-time domain dynamics at the velocity and impulse level, as is generally the case to avoid inconsistency [34]. Dynamics integration methods can be broadly classified according to explicit/implicit type and linear/non-linear type. In this work, we construct the dynamic equation in linearized implicit way, by mainly adopting the idea from passive midpoint integration [35]. There are two main reasons; 1) while targeting complex systems including flexible bodies,

the explicit method has clear limitations in its stability and 2) nonlinear integration can actually be expressed as an iteration of a linear integration. The equation of motion of mechanical system under contacts in the continuous-time domain is given by

$$\begin{aligned} M(q)\ddot{q} + C(q, \dot{q})\dot{q} + d\psi^T &= f_{ext} + J_c(q)^T \lambda_c \\ &= f_{ext} + \sum_{m=1}^{n_c} J_{c,m}(q)^T \lambda_{c,m} \end{aligned} \quad (3)$$

where  $q \in \mathbb{R}^n$  is the generalized coordinate variable of system involving any representation for rigid and deformable bodies,  $M(q), C(q, \dot{q}) \in \mathbb{R}^{n \times n}$  are the mass, Coriolis matrix,  $d\psi^T \in \mathbb{R}^n$  is the potential action,  $f_{ext} \in \mathbb{R}^n$  is the external force,  $\lambda_c = [\lambda_{c,1}; \dots; \lambda_{c,n_c}]$  with  $\lambda_{c,m} = [\lambda_{n,m}; \lambda_{t_1,m}; \lambda_{t_2,m}]$ ,  $J_c = [J_{c,1}; \dots; J_{c,n_c}]$ , and subscripts  $n, t_1, t_2$  denote the normal and tangential directions. Then the discretized version of the dynamics is

$$\begin{aligned} M_k \frac{v_{k+1} - v_k}{t_k} + C_k v_k + d\psi_k^T &= f_{ext,k} + J_{c,k}^T \lambda_{c,k} \\ \hat{v}_k &= \frac{v_k + v_{k+1}}{2}, \quad q_{k+1} = q_k + \hat{v}_k t_k \end{aligned} \quad (4)$$

where  $k$  denotes the time step index,  $M_k = M(q_k)$ ,  $C_k = C(q_k, v_k)$ ,  $t_k$  is the step size,  $v_k \in \mathbb{R}^n$  is the velocity, and  $\hat{v}_k$  is the representative velocity of each time step. Following to [35], potential action can be derived from the passivity relation i.e.,

$$d\psi_k^T \hat{v}_k t_k = \frac{\partial \psi}{\partial q_k} \hat{v}_k t_k + \frac{1}{2} \hat{v}_k^T \frac{\partial^2 \psi}{\partial q_k^2} \hat{v}_k t_k^2 \quad (5)$$

$$\approx \psi_{k+1} - \psi_k \quad (6)$$

with the second-order approximation of exact potential energy deviation. Here, potential function may be non-convex therefore the Hessian term may not be symmetric positive definite. Yet, some common approximations can be adopted to solve the issue in a compact way. Consider the following constraint potential form:

$$\psi(q) = \frac{1}{2} e(q)^T K(q) e(q) \quad (7)$$

where  $e(q) \in \mathbb{R}^{n_e}$  is the constraint error and  $K(q) \in \mathbb{R}^{n_e \times n_e}$  is the symmetric positive definite gain matrix, and  $n_s$  is the constraint dimension. This form (7) is very versatile, as it can represent almost all types of constraint including simple spring, co-rotational finite element model [36] and even hyper-elastic material with generalized compliance model [33]. Then we can write as follow using outer approximation similar to [31], [33], [37]:

$$\begin{aligned} \frac{\partial \psi}{\partial q} &\approx J_e(q)^T K(q) e(q) \\ \frac{\partial^2 \psi}{\partial q^2} &\approx J_e(q)^T K(q) J_e(q) + E(q) \end{aligned} \quad (8)$$

where  $J_e(q) \in \mathbb{R}^{n_e \times n}$  is the constraint Jacobian (i.e.,  $\frac{\partial e}{\partial q}$ ) and  $E(q) \in \mathbb{R}^{n \times n}$  is the symmetric positive definite damping matrix. To maintain the exact energy relation along these approximations (or at least, stability preserved), determining  $E(q)$  is another meaningful subject, as it is necessary to find

an appropriate energy dissipation to preserve the passivity of the system. Yet in this paper, we do not delve deep into this issue and apply the following two simple policies: 1) user-defined constant damping matrix or 2) symmetric positive definite projection of geometric stiffness matrix [37] i.e.,

$$E(q) = \text{proj}_{\text{SPD}} \left[ \frac{\partial J_e}{\partial q} K(q) e(q) \right]$$

where  $\text{proj}_{\text{SPD}}$  is the projection to symmetric positive definite manifold. One of classical ways to compute  $\text{proj}_{\text{SPD}}$  uses singular value decomposition [38], however, to reduce the computation time for this, we construct a diagonal matrix where each element is the sum of the absolute values of the elements in each column of the original matrix.

One of the widely used potentials that cannot be represented by (7) is gravity potential, however, its Hessian can be ignored by dropping out the derivative of the  $J_e(q)$  as above. Finally, substituting (8) to (4), dynamics can be represented as in form of (1) with

$$\begin{aligned} A_k &= \hat{M}_k + \frac{1}{2} (J_e(q_k)^T K(q_k) J_e(q_k) + E(q_k)) t_k \\ b_k &= \hat{M}_k v_k - C(q_k, v_k) v_k - J_e(q_k)^T K(q_k) e(q_k) + f_{ext,k} \end{aligned} \quad (9)$$

where  $\hat{M}_k = 2t_k^{-1} M_k$ . Although some approximations for non-linear potential action are used in our formulation, still it is much more stable than other explicit methods which take only first-order term of (5) and therefore, the formulation is applicable to complex multibody systems including rigid and deformable bodies. Also here, note that  $A_k$  is always a symmetric positive definite matrix.

The form of (1) is very common and also applicable to the general integration method. For example, coordinate transform using  $M(q)^{\frac{1}{2}}$  introduced in [35] can be utilized to improve the passivity property of the dynamics, as it maintains the linearized form with symmetric positive definite property of  $A_k$ . For the cases of non-linear integration, that takes constraints into account a completely implicit manner without linearization, we can write the equation as the form of

$$g(\hat{v}_k) = 0$$

where  $g : \mathbb{R}^n \rightarrow \mathbb{R}^n$  is the non-linear function. For instance, for fully-implicit Euler integration [29],  $g(\hat{v}_k)$  is

$$M_k \frac{v_{k+1} - v_k}{t_k} + C_k v_k + \nabla \psi(\hat{q}_k) - f_{ext,k} - J_{c,k}^T \lambda_{c,k}$$

with  $\hat{v}_k = v_{k+1}$ ,  $\hat{q}_k = q_k + \hat{v}_k t_k$ . Similarly, implicit midpoint integration [39], variational integration [40] can be represented. Then solving this equation using the Newton method is equivalent to

$$\hat{v}_k \leftarrow \hat{v}_k - \frac{\partial g}{\partial \hat{v}_k} g(\hat{v}_k) \quad (10)$$

and (10) can be simplified as

$$A_k \hat{v}_k = b_k + J_{c,k}^T \lambda_{c,k}$$

which is same as (1). Here,  $A_k$  is an symmetric positive definite matrix, with some quasi-Newton style approximation. Therefore, our framework does not restricted by the type of the

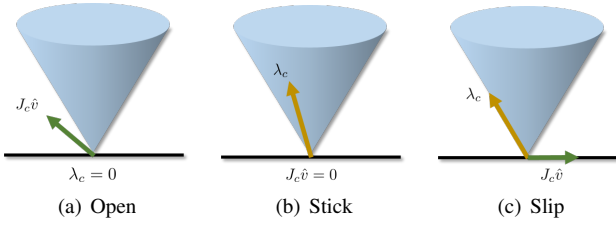


Fig. 1: Three cases induced from SCC. Blue shape represents friction cone set, green line denotes contact frame velocity and yellow line denotes contact impulse.

integration. However, still, there remains room for expansion to be directly applicable to the nonlinear integration methods, especially those that can be expressed in an optimization form [29]. However, we will remain the part as a future work.

It is worth mentioning that Featherstone algorithm [41] or a method using preconditioner [42] on  $A_k$  is not applicable for the complex system including rigid and deformable bodies, since they rely on the specific structure of the system (e.g., articulation, explicit-type constraints). This means ‘tricks’ for inversion (or factorization) of  $A_k$  is hard to be applied to general multibody dynamics.

### B. Signorini-Coulomb Condition

To precisely reflect the physical properties of the contact with its complementary nature, we consider solving the constructed dynamics (1) under the following Signorini-Coulomb condition (SCC):

$$\begin{aligned} 0 &\leq \lambda_{n,m} \perp J_{n,m} \hat{v} + \phi_{n,m} \geq 0 \\ 0 &\leq \delta_m \perp \mu \lambda_{n,m} - \|\lambda_{t,m}\| \geq 0 \\ \delta_m \lambda_{t,m} + \lambda_{n,m} J_{t,m} \hat{v} &= 0 \end{aligned} \quad (11)$$

for all contact index  $m = \{1, \dots, n_c\}$  where  $\mu$  is the friction coefficient,  $\phi_{n,m} \in \mathbb{R}^1$  is the additional term for penetration compensation and restitution coefficient, and  $\delta_m \in \mathbb{R}^1$  is the auxiliary variable. The first line of (11) is known as the Signorini condition which prevents penetration in a collision. The rest parts correspond to the Coulomb friction condition that ensures the contact impulse contained within the friction cone set defined as

$$\mathcal{C}_\lambda = \{\lambda_n, \lambda_t \mid \lambda_n \geq 0, \mu \lambda_n - \|\lambda_t\| \geq 0\} \quad (12)$$

and tangential impulse operates in the opposite direction of motion if sliding occurs. There are three possible behavior outcomes as the result of this condition, which are illustrated in Fig. 1 - open ( $\lambda_{n,m} = 0$ ), stick ( $\lambda_{n,m} > 0, \delta_m = 0$ ), and slip ( $\lambda_{n,m} > 0, \delta_m > 0$ ).

### III. DYNAMICS SOLVER

The main idea of COND is to replace the original problem (i.e., solve (1) with (11)) with the repetitions of surrogate contact problem (i.e., solve surrogate dynamics with (11)). In this section, we will describe how the surrogate dynamics contact problems are constructed and solved, with the concept of contact nodalization and diagonalization.

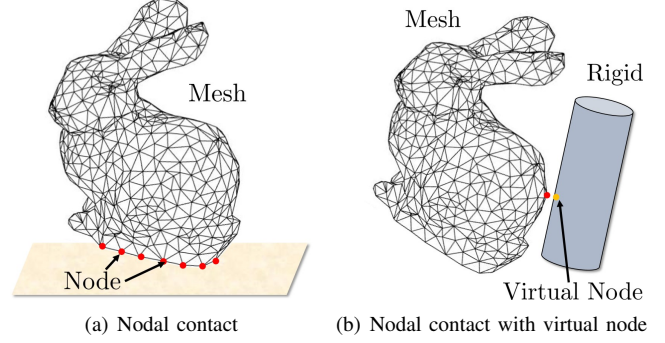


Fig. 2: Schematic of nodal contact situation. Red points are the nodes that originally exists in the mesh. Orange point is a virtual node that temporarily generated on rigid body.

#### A. Contact Nodalization

Contact nodalization assures that every point on which the contact acts corresponds to a node in the system, using the concept of virtual node. The details are described below.

1) *Nodal contact assumption*: An example of nodal contact is illustrated in Fig. 2(a). In this paper, we categorize contacts into two types according to the following definitions:

*Definition 1*: For any point of contact, it is an S-contact, if it is a part of collision between an dynamic object and a static environment. Otherwise, it is a D-contact, which is a part of collision between two dynamic objects.

Under nodal contact assumption, S-contact is a static-node contact, while D-contact is a node-node contact.

Based on this, we can take the important observation that the contact Jacobian  $J_c$  in the nodal situation can be represented by the stack of SO(3):

$$\begin{cases} J_{c,m} = [0, \dots, R_{c,m}, \dots, 0] & \text{if S-contact} \\ J_{c,m} = [0, \dots, R_{c,m}, \dots, -R_{c,m}, \dots, 0] & \text{if D-contact} \end{cases} \quad (13)$$

where  $R_{c,m} \in \mathbb{R}^{3 \times 3}$  is the SO(3) matrix for  $m$ -th contact that converts global frame to nodal contact frame. The assumption is sufficiently reasonable in fine mesh-based systems, but in general, nodal contact situations alone cannot express all the situations that occur in multibody interaction. Few previous studies have dealt with the limitation of nodal contact for a specific application as the work in [32] utilized adaptive meshing for cloth simulation to deal with fine contact, and [30] defined additional assumptions that can be applied to thin nodal objects. The main limitation of above approaches is that it applies only to specific areas (especially not for rigid bodies). However since we aim at robotic applications, we develop a method that can deal with more general situations.

2) *Virtual node*: To embrace the broad contact situation as nodal, we make the concept of the virtual node as shown in Fig. 2(b). The mass-less virtual node is temporarily formed when contact occurs if the point is not a predefined node and the contact is treated as occurring on the virtual node. By this, all the contacts that exist in the system can be fairly considered as nodal contacts. However, for virtual node concept to be valid, the motion of the virtual node and the point where the

contact originally occurred must match. To implement this, we utilize viscous damping force between the virtual nodes and collision points:

$$f_v = -k_v(J_v\hat{v} - \hat{v}_v) \quad (14)$$

where  $k_v$  can be interpreted as a gain,  $J_v \in \mathbb{R}^{3n_v \times n}$  is the Jacobian matrix that maps the velocity of the original coordinate to collision point velocity, and  $\hat{v}_v \in \mathbb{R}^{3n_v}$  is the representative velocity of virtual nodes while  $n_v$  is the number of virtual nodes. Note that damping force is sufficient to match the motion since the virtual nodes are created at the ‘exact’ locations (i.e., no constraint error) at every time step and disappears at the next time step. Virtual nodes can be generated on any part of the system (e.g., surface on rigid body, interior points between mesh nodes) by simply create a mapping from the original coordinate to the location of the node.

Based on (14), we can reformulate the original dynamics as

$$\underbrace{\begin{bmatrix} A_o + k_v J_v^T J_v & -k_v J_v^T \\ -k_v J_v & k_v I \end{bmatrix}}_{=A} \underbrace{\begin{bmatrix} \hat{v}_o \\ \hat{v}_v \end{bmatrix}}_{=\hat{v}} = \underbrace{\begin{bmatrix} b_o \\ 0 \end{bmatrix}}_{=b} + \underbrace{\begin{bmatrix} J_{co}^T & 0 \\ 0 & J_{cv}^T \end{bmatrix}}_{=J_c^T} \underbrace{\begin{bmatrix} \lambda_{co} \\ \lambda_{cv} \end{bmatrix}}_{=\lambda_c} \quad (15)$$

where  $A_o, b_o$  are from original dynamics,  $\lambda_{co}, \lambda_{cv}, J_{co}$ , and  $J_{cv}$  are respectively the contact impulse on original/virtual nodes and contact Jacobian on original/virtual nodes. Note that (15) is structurally identical to (1). Prop. 1 provides a rationale that our virtual node formulation is reasonable - symmetric positive definite property of dynamic matrix is preserved and the solution converges to it of original formulation solution if  $k_v$  is large enough.

*Proposition 1:*  $A$  in (15) is a symmetric positive definite matrix. Also, the contact formulation using virtual nodes converges to the original contact formulation as  $k_v \rightarrow \infty$ .

*Proof:* Since  $A_o$  is a symmetric positive definite matrix,  $A$  is at least symmetric and positive semi-definite. Now suppose that  $x = [x_1; x_2]$  exists that satisfies  $x^T A x = 0$ . Then  $x_1$  must be zero vector to make  $x_1^T A_o x_1 = 0$ . Then  $x^T A x = k_v x_2^T x_2 = 0$  holds, which show  $x_2$  is also a zero vector and it denotes  $A$  is positive definite. Also from (15), we can obtain

$$\begin{aligned} A_o \hat{v}_o &= b_o - k_v J_v^T J_v \hat{v}_v - k_v J_v^T \hat{v}_v + J_{co}^T \lambda_{co} \\ &= b_o + J_v^T J_{cv}^T \lambda_{cv} + J_{co}^T \lambda_{co} \end{aligned} \quad (16)$$

This means that the dynamics for ‘original’ system does not change even if a virtual node is used. Meanwhile, contact on virtual nodes leverages the relation between

$$J_{cv} \hat{v}_v = J_{cv} (J_v \hat{v}_o + k_v^{-1} J_{cv}^T \lambda_{cv})$$

and  $\lambda_{cv}$ . Also, contact condition implies dissipative property (normal complementarity, opposite friction direction) so

$$\lambda_{cv}^T J_{cv} (J_v A_o^{-1} J_v^T + k_v^{-1} I) J_{cv}^T \lambda_{cv} + \lambda_{cv}^T J_{cv} J_v A_o^{-1} b'_o \leq 0$$

with  $b'_o = b_o + J_{co}^T \lambda_{co}$  has to be hold. Then if  $k_v^{-1} J_{cv}^T \lambda_{cv}$  does not converges to 0 as  $k_v \rightarrow \infty$ , it denotes  $J_{cv}^T \lambda_{cv}$  goes to infinity and condition cannot be satisfied since  $J_v A_o^{-1} J_v^T + k_v^{-1} I$  is a symmetric positive definite matrix. Therefore as  $k_v \rightarrow \infty$ , virtual node based contact formulation converges to original contact formulation as it leverages the relation between  $J_{cv} J_v \hat{v}$  and  $\lambda_{cv}$ . ■

It is important to note that in (14), utilizing representative velocity as in [35] is critical, as it leads (16) to preserve the structure of  $A_o, B_o$ . As a result, even with sporadic generation of multiple virtual nodes and high  $k_v$ , the formulation can maintain the stability. Our virtual node-based formulation is similar to a concept of slack variable, so may has a disadvantage that the dimension of the system increases as the number of non-nodal contact increases. Nonetheless, the nodal transformation substantially contributes to our algorithm to reduce the burden of the  $\mathcal{O}(n^3)$  operation in standard methods [43] - which will be explained in more detail below.

### B. VL-FPI with Surrogate Dynamics

Let us first consider solving (15) with only Signorini condition in (11). Then we can find that it is equivalent to Karush–Kuhn–Tucker (KKT) conditions of following velocity-level optimization problem:

$$\begin{aligned} \min_{\hat{v}} \quad & \frac{1}{2} \hat{v}^T A \hat{v} - b^T \hat{v} \\ \text{s.t.} \quad & \hat{v} \in \mathcal{C}_V \end{aligned} \quad (17)$$

where  $\mathcal{C}_V = \{\hat{v} \mid J_n \hat{v} + \phi_n \geq 0\}$  is the feasible set of velocity with  $\phi_n = [\phi_{n,1}, \dots, \phi_{n,m}]^T$ . Here and hereafter, notations for  $k$ -th time step are omitted for simplification, however all the components are still time-varying. This means that contact problems without friction can be replaced with solving (17). One way to solve (17) is the projected gradient descent method [44] which takes the following steps:

$$\hat{v}^* \leftarrow \hat{v}^l - W(A\hat{v}^l - b) \quad (18)$$

$$\hat{v}^{l+1} \leftarrow \Pi_{\mathcal{C}_V}(\hat{v}^*) \quad (19)$$

where  $l$  is the iteration loop index,  $W \in \mathbb{R}^{n \times n}$  is the weight matrix for gradient descent, and  $\Pi(\cdot)$  is the Euclidean projection operator [44] defined as

$$\Pi_{\mathcal{C}_V}(x) = \arg \min_{y \in \mathcal{C}_V} \frac{1}{2} \|y - x\|^2$$

which is the closest point from  $x$  on the convex set  $\mathcal{C}_V$ . Since  $A$  is positive definite and  $\mathcal{C}_V$  is convex, the projected gradient descent method will well converge to the solution of (17) if the problem is feasible. However, since (11) also include the impulse-level constraint like friction direction constraint, it is not enough to deal with the generic contact problem.

To overcome this issue, we modify the projection step (19) as follow:

$$W^{-1} \hat{v}^{l+1} \leftarrow W^{-1} \hat{v}^* + J_c^T \lambda_c \quad (20)$$

where  $\lambda_c$  is the solution of the following contact problem:

$$\begin{aligned} \text{Solve } & J_c \hat{v}^{l+1} = \Gamma_c \lambda_c + \eta_c \\ \text{subject to } & (11) \end{aligned} \quad (21)$$

where  $\Gamma_c = J_c W J_c^T \in \mathbb{R}^{3n_c \times 3n_c}$  and  $\eta_c = J_c \hat{v}^* \in \mathbb{R}^{3n_c}$ . Here, noticing the similarity between (20) and (1), (20) can be considered as a ‘surrogate’ dynamics, which is constructed from  $W$  and  $\hat{v}^*$ . Then (21) can be interpreted as the contact problem with respect to this surrogate dynamics, similar to a form of (2) while  $\Gamma_c$  can be interpreted as a surrogate Delassus

operator. After solving this contact problem (21), update step is performed as

$$\hat{v}^{l+1} \leftarrow \hat{v}^* + WJ_c^T \lambda_c \quad (22)$$

Although projection step in projected gradient descent only enforce velocity-level constraint, this new velocity-level fixed point iteration (i.e., iteration of (18), (21) and (22)) directly achieves the contact condition (11) between  $\hat{v}^{l+1}$  and  $\lambda_c$ , yet does not satisfy the dynamics condition (15). However, if the fixed-point iteration converges,

$$\hat{v}^{l+1} = \hat{v}^l - W(A\hat{v}^l - b) + WJ_c^T \lambda_c = \hat{v}^l$$

holds and it is equivalent to

$$A\hat{v}^l = b + J_c^T \lambda_c$$

as  $W$  is a weight matrix which is supposed to be a non-singular matrix. Therefore, we can find that hypothetical formula (20) eventually accurately reflects the dynamics condition if the iteration converges - the convergence properties will be discussed later in Sec. IV.

### C. Contact Diagonalization

In our VL-FPI process above, computing  $\hat{v}^*$  step (18) and updating  $\hat{v}^{l+1}$  step (22) are simple processes, yet the part that solves surrogate contact problem (21) may be complicated. However, we find that selecting an appropriate weight matrix (i.e.,  $W$ ) under contact nodalization can make our surrogate Delassus operator  $\Gamma_c = J_c W J_c^T$  to be a diagonal matrix for all situations and the process can be drastically simplified. The proposition below demonstrates how it works.

*Proposition 2:* Under contact nodalization, suppose

$$W = \text{diag}(w_{11}, \dots, w_{nn})$$

with  $w_{i_1 i_1} = w_{i_2 i_2} = w_{i_3 i_3} = \bar{w}_i \in \mathbb{R}^1$  for all  $i$ -th node that is in contact, where  $i_1, i_2, i_3$  are indices corresponding to the node. Then the surrogate Delassus operator  $\Gamma_c$  can be written as follow:

$$\begin{aligned} \Gamma_c &= \text{diag}(\Gamma_{c,1}, \dots, \Gamma_{c,n_c}) \\ &= \text{diag}(\gamma_{c,1} I_{3 \times 3}, \dots, \gamma_{c,n_c} I_{3 \times 3}) \\ \gamma_{c,m} &= \begin{cases} \bar{w}_i, & \text{if } i\text{-th node is in S-contact} \\ \bar{w}_i + \bar{w}_j, & \text{if } i, j\text{-th node are in D-contact} \end{cases} \end{aligned}$$

where  $I$  denotes the identity matrix.

*Proof:* Recalling (13), the proof is simply derived from the fact that

$$\bar{R} \bar{W} \bar{R}^T = \bar{w} \bar{R} \bar{R}^T = \bar{W}$$

holds for  $\bar{W} = \bar{w} I \in \mathbb{R}^{3 \times 3}$  with a scalar  $\bar{w}$  and SO(3) matrix  $\bar{R} \in \mathbb{R}^{3 \times 3}$ . ■

Prop. 2 demonstrates that under certain structure of  $W$ , extracting the components of  $W$  is sufficient to construct the surrogate Delassus operator, without any matrix-matrix multiplication or inversion. Therefore, we can obtain significant advantages in time and memory compare to original Delassus operator (i.e.  $J_c A^{-1} J_c^T$ ) assembly. Also, the simple

---

### Algorithm 1 COND

---

```

1: while Simulation loop do
2:   Construct original dynamics
3:   Perform collision detection with contact nodalization
4:   Construct dynamics  $A, b, J_c$  based on (15)
5:   Initialize  $\hat{v}^1$ 
6:   while VL-FPI loop do
7:      $l \leftarrow l + 1$ 
8:     Determine step size matrix  $W$ 
9:      $\hat{v}^* \leftarrow \hat{v}^l - W(A\hat{v}^l - b)$ 
10:    Construct  $\Gamma_c$  based on diagonalized property
11:    Solve (21) using Alg. 2
12:     $\hat{v}^{l+1} \leftarrow \hat{v}^* + WJ_c^T \lambda_c$ 
13:    Compute residual  $\theta = \|\hat{v}^{l+1} - \hat{v}^l\|$ 
14:    if  $\theta < \theta_{th}$  or  $l = l_{max}$  then
15:      break
16:    end if
17:  end while
18:  Update state using  $\hat{v}^{l+1}$ 
19: end while

```

---

structure of Delassus operator is significantly advantageous for the contact solving process (see Sec. III-D).

With this contact ‘diagonalization’ method, we have built the basic structure of our simulation algorithm - COND, which is summarized in Alg. 1.

### D. Surrogate Dynamics Contact Solver

Now the remaining part is how to solve (21). In typical solvers, although the contact conditions (11) are constraints that are independent with each contact, coupling between each contact is still exists since the Delassus operator is dense. These coupling terms make the global iteration and relaxation process essential for contact solvers when dealing with multi-contact situations [14], [15]. However, in COND, the diagonalized property of  $\Gamma_c$  established in Sec. III-B resolves this problem. Convenience induce from the property of  $\Gamma_c$  in the contact solving process can be summarized as follows:

- Coupling relaxation through global iteration (e.g., Gauss-Seidel) is unnecessary since each contact situation is completely decoupled. Furthermore, completely parallel computation is possible for each contact.
- Even for each single contact problem, coupling between normal and tangential impulse does not exist and it leads the exact solution to be obtained in more simple manner compare to without the need of numerical methods such as bisection [15], Newton [16], etc.

Overall, our contact solver consists only of a single linear solving of  $-\Gamma_c^{-1}$  (which is very simple since  $\Gamma_c$  is a diagonal matrix) with local projection step on  $\mathcal{C}_\lambda$ . We summarize this ‘one-shot’ contact solver in Alg. 2.

The friction cone projection step (denoted as ProjectFC in Alg. 2) is necessary to enforce the contact solver output to satisfy the SCC. If temporary value (i.e.,  $\lambda_{c,m}^*$  in Alg. 2) is inside  $\mathcal{C}_\lambda$ , ProjectFC simply yields the same value as input.

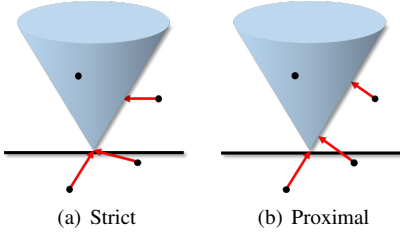


Fig. 3: Two ProjectFC schemes: strict and proximal. Black dot: value before projection, Red arrow: projection.

---

**Algorithm 2** One-shot contact solver
 

---

- 1: **for**  $m = 1$  to  $n_c$  **do in parallel**
  - 2:    $\lambda_{c,m}^* = -(\gamma_{c,m}I)^{-1}(\eta_{c,m} + \phi_{c,m})$
  - 3:    $\lambda_{c,m} = \text{ProjectFC}(\lambda_{c,m}^*)$
  - 4: **end for**
- 

Otherwise,  $\lambda_{c,m}^*$  is projected on the surface of  $\mathcal{C}_\lambda$ . In this paper, we use two projection schemes - ‘strict’ and ‘proximal’ operator as illustrated in Fig 3. Each can be written as

$$\begin{aligned} \text{Strict: } \lambda_{n,m} &= \max(\lambda_{n,m}^*, 0) \\ \lambda_{t,m} &= \Pi_{\mathcal{C}_{\lambda_{n,m}}}(\lambda_{t,m}^*) \\ \text{Proximal: } \lambda_{c,m} &= \Pi_{\mathcal{C}_\lambda}(\lambda_{c,m}^*) \end{aligned} \quad (23)$$

where  $\mathcal{C}_{\lambda_{n,m}}$  is the cross-section of  $\mathcal{C}_\lambda$  cut vertically from  $\lambda_{n,m}$ . It can be easily verified that for both strict operator and proximal operator, we can obtain the solution in very simple analytic form. Also note that  $\phi_c$  is only related to normal component, therefore  $\phi_{c,m} = [\phi_{n,m}, 0, 0]^T$ .

We figure out that the two projection schemes have the following trade-offs in our solver: 1) the result of strict operator exactly satisfies the SCC condition (11), yet sufficient condition for convergence is not always feasible<sup>1</sup> 2) proximal operator can always guarantee the convergence of the solver, yet the solution does not exactly satisfy (11). Also, in fact, the result from the proximal operator is equivalent to the convex contact model proposed in [21], [22], therefore has a unique solution under strong convexity and can achieve invertible property (i.e., contact impulse can reversely be calculated from the velocity result [22]), which is useful in trajectory optimization.

1) *Strict operator*: As mentioned above, strict operator can exactly achieve SCC in one-shot which is shown in Prop. 3.

*Proposition 3*: Output of Alg. 2 with the strict operator in (23) is the unique solution of (21).

*Proof*: From  $\Gamma_{c,m} = \gamma_{c,m}I_{3 \times 3}$ , normal component is completely decoupled from tangential component as

$$J_{n,m}\hat{v} = \gamma_{c,m}\lambda_{n,m} + \eta_{n,m}$$

where  $\eta_{c,m} = [\eta_{n,m}, \eta_{t1,m}, \eta_{t2,m}]^T$ . If  $\lambda_{n,m}^* > 0$ ,  $\lambda_{n,m} = \lambda_{n,m}^*$  is the only solution that  $J_{n,m}\hat{v} + \phi_{n,m} = 0$  is satisfied. Else,  $\lambda_{n,m} = 0$  is the only solution as  $J_{n,m}\hat{v} + \phi_{n,m} > 0$  since  $\gamma_{n,m} > 0$ . Therefore, normal components are uniquely

determined and satisfy the complementarity condition is satisfied. For tangential component, stick case is trivial. For slip case,

$$\begin{aligned} \gamma_{c,m}\lambda_{t1,m} + \eta_{t1,m} &= -\beta\lambda_{t1,m} \\ \gamma_{c,m}\lambda_{t2,m} + \eta_{t2,m} &= -\beta\lambda_{t2,m} \end{aligned} \quad (24)$$

must be satisfied for  $\beta > 0$ . Substituting (24) to boundary of  $\mathcal{C}_\lambda$ ,  $\beta$  is uniquely determined as

$$\beta = -\gamma_{c,m} + \frac{\|\lambda_{t,m}\|}{\mu\lambda_{n,m}}$$

and therefore  $\lambda_{t,m}$  is uniquely determined and equivalent to the result of the strict operator. ■

2) *Proximal operator*: As depicted in Fig. 3, a result of the proximal operator is slightly different from the strict operator, which implies that the proximal operator-based formulation contains some approximation in SCC. We first analyze the condition that the result of the proximal operator entails in Prop. 4.

*Proposition 4*: Output of Alg. 2 with the proximal operator in (23) is the unique solution of (21) with following relaxed SCC instead of (11):

$$\begin{aligned} 0 &\leq \lambda_{n,m} \perp J_{n,m}\hat{v} + \phi_{n,m} - 2\vartheta\lambda_{n,m} \geq 0 \\ 0 &\leq \delta_m \perp \mu\lambda_{n,m} - \|\lambda_{t,m}\| \geq 0 \\ \delta_m\lambda_{t,m} + J_{t,m}\hat{v} &= 0 \end{aligned}$$

*Proof*: Proximal operator solves following optimization problem:

$$\lambda_{c,m} = \min_{\lambda} \frac{1}{2}\lambda^T\Gamma_{c,m}\lambda + \lambda^T(\eta_{c,m} + \phi_{c,m}) \quad \text{s.t.} \quad \lambda \in \mathcal{C}_\lambda \quad (25)$$

for all contact index  $m = \{1, \dots, n_c\}$ . Then KKT condition of the problem can be written as

$$J_{n,m}\hat{v} + \phi_{n,m} - \vartheta' - 2\vartheta\lambda_{n,m} = 0 \quad (26)$$

$$J_{t,m}\hat{v} + \vartheta(2\mu_1^{-2}\lambda_{t,m}) = 0 \quad (27)$$

$$\vartheta'\lambda_{n,m} = 0 \quad (28)$$

$$\vartheta(-(\lambda_{n,m})^2 + \mu^{-2}\|\lambda_{t,m}\|^2) = 0 \quad (29)$$

$$\vartheta, \vartheta' \geq 0 \quad (30)$$

$$\lambda_{c,m} \in \mathcal{C}_\lambda \quad (31)$$

for  $m = \{1, \dots, n_c\}$  where  $\vartheta, \vartheta'$  is the Lagrange multipliers. From (26), (28), and (30), we can find that

$$J_{n,m}\hat{v} + \phi_{n,m} - 2\vartheta\lambda_{n,m} = \vartheta' \geq 0$$

$$\lambda_{n,m}(J_{n,m}\hat{v} + \phi_{n,m} - 2\vartheta\lambda_{n,m}) = \vartheta'\lambda_{n,m} = 0$$

holds and it is equivalent to relaxed normal complementarity condition in the statement. For tangential component condition, open case is trivial from (31). Also from (29),  $\vartheta = 0$  holds for stick case and  $\|J_{t,m}\hat{v}\| = 0$  is satisfied. Finally, (27) is equivalent to the condition for slip case. Also, since (25) is the strictly convex optimization problem, the solution is unique. ■

Suppose that VL-FPI iteration with proximal operator converges, then original dynamics (1) is satisfied and

$$\begin{aligned} \Gamma_c\lambda_c + \eta_c + \phi_c &= \Gamma_c\lambda_c + J_c(\hat{v} - WJ_c^T\lambda_c) + \phi_c \\ &= A_c\lambda_c + b_c \end{aligned}$$

<sup>1</sup>From the fundamental limitation of SCC. In practice, we do not experience the convergence problem. For detail discussions and results, see Sec. IV.V.

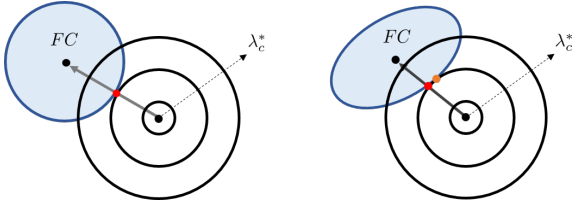


Fig. 4: Illustration of the projection result (orange) of strict operator for isotropic friction model (left) and anisotropic friction model (right). The solution with the friction direction opposite to the sliding direction (red) differs in anisotropic friction.

holds where  $A_c = J_c A^{-1} J_c^T$ ,  $b_c = J_c A^{-1} b + \phi_c$ . From this, we can find that converged solution of COND using proximal operator is equivalent to the solution of CCP [21] which can be written as

$$\begin{aligned} \lambda_c &= \min_{\lambda} \frac{1}{2} \lambda^T A_c \lambda + \lambda^T b_c \\ \text{s.t. } \lambda_m &\in \mathcal{C}_\lambda \quad m = \{1, \dots, n_c\} \end{aligned} \quad (32)$$

Compare the conditions in Prop. 4 with (11), we can find that Signorini condition is relaxed. Therefore, which is also shown in [14], the solution of CCP may generate unplausible dynamic behavior. However, as mentioned in [21], the moderate use of  $\phi$  can reduce the effect of the approximation of normal conditions, and in practice it is employed in well-known simulators such as MuJoCo [24] as it works quite robustly. Furthermore, with the regularization term added in (32), following formulation is derived:

$$\begin{aligned} \lambda_c &= \min_{\lambda} \frac{1}{2} \lambda^T (A_c + \Omega_c) \lambda + b_c^T \lambda \\ \text{s.t. } \lambda_m &\in \mathcal{C}_\lambda \quad m = \{1, \dots, n_c\} \end{aligned} \quad (33)$$

where  $\Omega_c \in \mathbb{R}^{3n_c \times 3n_c}$  is the symmetric positive definite regularization term. In [22], invertible property of (33) is shown as the contact impulse can be reversely calculated from the velocity result  $\hat{v}$  using following optimization:

$$\begin{aligned} \lambda_c &= \min_{\lambda} \frac{1}{2} \lambda^T \Omega_c \lambda + \lambda^T J_c \hat{v} \\ \text{s.t. } \lambda_m &\in \mathcal{C}_\lambda \quad m = \{1, \dots, n_c\} \end{aligned}$$

Since  $\Omega_c$  is a symmetric positive definite matrix, the problem is strictly convex. It can be easily verified that (33) is also solvable using our framework by simply using  $\Gamma_c + \Omega_c$  instead of  $\Gamma_c$  in (21).

*Remark 1 (Overall exactness):* The solution of surrogate dynamics contact problem solved by Alg. 2 at each VL-FPI iteration will satisfy SCC with respect to the surrogate dynamics. As stated in Sec. III-B, when the VL-FPI converges, surrogate dynamics will accurately reflect (15). Therefore, the solution will be equivalent to the solution of the original problem.

### E. Anisotropic Friction

So far, we focus on isotropic friction model, which use the same  $\mu$  for all directions. However in some cases, anisotropic friction modeling is necessary [45]. For example, ellipsoidal

cone as

$$\mathcal{C}_\lambda = \left\{ \lambda_n, \lambda_t \mid \lambda_n \geq 0, \lambda_n^2 \geq \frac{\lambda_{t_1}^2}{\mu_1^2} + \frac{\lambda_{t_2}^2}{\mu_2^2} \right\}$$

may have to be adopted. We find that due to our diagonalization process, anisotropic friction cones can also be accommodated conveniently. In fact, this can be done without any additional modification of the operator, because the solution from strict operator exactly satisfies the maximal dissipation principle (MDP [46]), as shown in Prop. 5.

*Proposition 5:* Output of Alg. 2 with the strict operator is the maximal dissipation solution.

*Proof:* Maximal dissipation principle can be written as

$$\begin{aligned} \lambda_{c,m} &= \min_{\lambda} \frac{1}{2} \lambda^T \Gamma_{c,m} \lambda + \lambda^T (\eta_{c,m} + \phi_{c,m}) \\ \text{s.t. } \lambda_n &\perp J_{n,m} \hat{v} + \phi_{n,m}, \quad \lambda \in \mathcal{C}_\lambda \end{aligned}$$

for  $m = \{1, \dots, n_c\}$ . We can easily find that the cost function in MDP is proportional to the square of distance from  $\lambda_{t,m}^*$  as in Fig. 4 while the normal component is already determined to satisfy the Signorini condition. Therefore, the optimal solution is equivalent to the minimum distance projection result. ■

As is known, in the case of anisotropic friction, the MDP is not equivalent to that the friction is in the opposite of the direction which is also depicted in Fig. 4. In the anisotropic case, the projection result of the strict operator may not be represented analytically, and numerical methods (e.g., bisection) may be required. However by supporting parallelization for all contacts, this can be solved without bottleneck.

### F. Complexity

Summarizing the preceding contents, it is established that all components of VL-FPI in COND (Alg. 1) are made up of simple scalar algebraic operations and matrix-vector multiplication. More precisely, the first multiplication of  $W$  in (20) and (22) has  $\mathcal{O}(n)$  complexity for both time and space since  $W$  is a diagonal matrix. One-shot contact solving process (Alg. 2) also possess  $\mathcal{O}(n)$  complexity since construction of  $\Gamma_c$  does not involves any multiplication, but only element extraction from  $W$ , while contact solving is interpreted as  $n_c$  (usually proportional to  $n$ ) number of simple parallelizable operations. Also, since  $J_c$  can be treated as just a stack of SO(3) matrices, matrix-vector multiplication on  $J_c$  has also  $\mathcal{O}(n)$  complexity. Therefore, the only part that have over linear complexity is a computation of  $A \hat{v}^l$ . Matrix-vector multiplication requires  $\mathcal{O}(n^2)$  complexity if  $A$  is dense, but in many cases, especially for deformable body parts,  $A$  contains many 0 components. As a result, COND shows the complexity near  $\mathcal{O}(n)$  - see Sec. V. Note that despite  $A$  is sparse,  $A^{-1}$  is generally fully dense, therefore computation of  $J_c A^{-1} J_c^T$  is still has a complexity near  $\mathcal{O}(n^3)$ .

### G. Chebyshev Acceleration

We find that Chebyshev acceleration [47] can be utilized as a efficient plug-in to accelerate the VL-FPI in COND. For iterate linear solver to solve  $A \hat{v} = b$  defined as

$$\hat{v}^{l+1} = A_1^{-1} (A_2 \hat{v}^l - b)$$



---

**Algorithm 3** VL-FPI with Chebyshev acceleration
 

---

```

1: while VL-FPI loop do
2:    $l \leftarrow l + 1$ 
3:   Determine step size matrix  $W$ 
4:    $\hat{v}^* \leftarrow \hat{v}^l - W(A\hat{v}^l - b)$ 
5:   Construct  $\Gamma_c$  based on diagonalized property
6:   Solve (21) using Alg. 2
7:    $\hat{v}^{**} \leftarrow \hat{v}^* + WJ_c^T \lambda_c$ 
8:    $\nu_{l+1} = \begin{cases} 1 & \text{if } l < l_s \\ \frac{2}{2-\varrho^2} & \text{if } l = l_s \\ \frac{4}{4-\varrho^2\nu_l} & \text{if } l > l_s \end{cases}$ 
9:    $\hat{v}^{l+1} \leftarrow \nu_{l+1}(u(\hat{v}^{**} - \hat{v}^l) + \hat{v}^l - \hat{v}^{l-1}) + \hat{v}^{l-1}$ 
10:  Compute residual  $\theta = \|\hat{v}^{l+1} - \hat{v}^l\|$ 
11:  if  $\theta < \theta_{th}$  or  $l = l_{max}$  then
12:    break
13:  end if
14:  Compute  $\varrho$  using (34)
15: end while

```

---

where  $A = A_1 - A_2$ , Chebyshev acceleration method proposes iteration scheme as

$$\hat{v}^{l+1} = \nu_{l+1}(A_1^{-1}(A_2\hat{v}^l - b) - \hat{v}^{l-1}) + \hat{v}^{l-1}$$

with

$$\nu_{l+1} = \frac{2P_l(\frac{1}{\varrho})}{\varrho P_{l+1}(\frac{1}{\varrho})}$$

where  $P$  denotes the Chebyshev polynomial and  $\varrho$  is the spectral radius of  $A_1^{-1}A_2$ . Looking closely at Alg. 1, we can find that our solver is quite similar to the linear solving scheme with  $A_1 = -W^{-1}$ ,  $A_2 = W^{-1} - A$ . Therefore, it can be expected that applying Chebyshev acceleration to COND will be effective. The algorithm is clarified in Alg. 3.

Here,  $l_s$  is the index for ‘slowly’ start acceleration as in [47] which is helpful to avoid oscillation at the beginning of the iteration. Also, since spectral radius  $\varrho$  is equivalent to the largest of the absolute values of the eigenvalues, its time complexity becomes an issue for a large size matrix. For this reason, we use a simple approximation of it instead as

$$\varrho = \min\left(\frac{\|\hat{v}^l - \hat{v}^{l-1}\|}{\|\hat{v}^{l-1} - \hat{v}^{l-2}\|}, 1\right) \quad (34)$$

Intuitively, this formulation reflects the degree of a contraction property, which is directly related to the spectral radius. The min operator is necessary because monotonic decreasing of residual is not always guaranteed with the acceleration schemes. In practice, when Chebyshev acceleration is applied, the residual of VL-FPI reduces much faster, yet with some chattering. To reduce the resulting instability, we utilize the under-relaxation strategy (i.e.,  $0 < u < 1$  in Alg. 3) which is proposed in [47].

#### IV. CONVERGENCE ANALYSIS

In this section, sufficient conditions for convergence of VL-FPI in COND will be discussed concretely. We first utilize

the Banach Fixed-Point Theorem [48] as a basis to discuss convergence i.e.,

*Lemma 1 (Banach Fixed-Point Theorem [48]):* If  $f : X \rightarrow X$  is a contraction mapping on non-empty complete metric space, fixed-point iteration  $x \leftarrow f(x)$  always converges to a unique fixed-point.

Remind that our functional representation of iteration process is written as

$$\begin{aligned} f(\hat{v}) &= (I - WA)\hat{v} + WJ_c^T \lambda_c \\ &= \hat{v}^* + WJ_c^T \lambda_c \end{aligned}$$

Here  $\lambda_c$  is the function of  $\hat{v}^*$ , yet cannot be expressed analytically in usual cases. However, our one-shot contact solver described in Sec. III-D facilitates access to this difficulty.

*Definition 2:* VL-FPI in COND is contractible, if the contraction property of the iteration can be guaranteed under proper step size matrix  $W$ .

By Lemma 1, if we show contractibility of VL-FPI, it implies that the iteration always converges and the problem has unique solution. We find that exact and proximal operators exhibit different mathematical properties so the analysis for each will be dealt with separately. Note that we use 2-norm as a distance metric so further notation of  $\|\cdot\|$  denotes 2-norm of a matrix/vector. Also,  $\sigma(\cdot)$  will refer eigenvalues of the matrix, and  $\bar{v}_i = [\hat{v}_{i1}, \hat{v}_{i2}, \hat{v}_{i3}]^T$  will indicate representative velocity of  $i$ -th node.

*Remark 2 (Nodalization):* The contact acts only on the (virtual) nodes among the total system degrees of freedom. For this reason, the value of the elements of  $f(\hat{v})$  other than the indices of the node to which the contact acts is equal to that of  $\hat{v}^*$  - the description of the corresponding content will be omitted in the proofs.

##### A. Strict Operator

Since the strict operator gives the solution that exactly satisfy SCC, it means that if our VL-FPI always converges, there is always a solution to the original contact problem. However, feasibility and uniqueness of the contact NCP solution are cannot be always guaranteed [46], [49]. For this reason, dealing with entire convergence for the strict operator is a fundamentally hard problem, unlike the proximal operator case (which will be explained later). Therefore, in this paper, we consider specific type of system.

*Definition 3:* A system is a completely-nodal system, if the system is composed only of particle nodes, and contact only acts on the nodes.

Even if a definition of completely-nodal system does not cover all commonly used system dynamics expressions, it can ‘represent’ any system by adopting sufficiently large number of nodes. We find that for completely-nodal system with sufficiently small time step, contractibility of VL-FPI can be guaranteed. For this, we first present following lemma.

*Lemma 2:* Strict operator is a Lipschitz continuous function.

*Proof:* From the property that projection on convex set is contraction [50] (and therefore, Lipschitz continuous), we can find that max operator is Lipschitz continuous, as  $\lambda_n \geq 0$  is the

invariant convex set. Therefore, we only need to show  $\Pi_{\mathcal{C}_{\lambda_n, m}}$  is Lipschitz continuous. Suppose two inputs of  $\Pi_{\mathcal{C}_{\lambda_n, m}}$  are  $\lambda_1^* = [\lambda_{1,n}^*; \lambda_{1,t_1}^*; \lambda_{1,t_2}^*]$  and  $\lambda_2^* = [\lambda_{2,n}^*; \lambda_{2,t_1}^*; \lambda_{2,t_2}^*]$  with outputs are  $\lambda_1$  and  $\lambda_2$  correspond to each. Now consider following triangular inequality:

$$\|\lambda_1 - \lambda_2\| \leq \|\lambda_1 - \lambda_3\| + \|\lambda_2 - \lambda_3\|$$

with  $\lambda_3^* = [\lambda_{2,n}^*; \lambda_{1,t_1}^*; \lambda_{1,t_2}^*]$  and output  $\lambda_3$ . Then we can prove each of the following two:

- $\|\lambda_1 - \lambda_3\| \leq \zeta \|\lambda_1^* - \lambda_3^*\|$  for finite constant  $\zeta$

If  $\lambda_1^*, \lambda_3^* \in \mathcal{C}_\lambda$ , it is trivial. If  $\lambda_1^*, \lambda_3^* \notin \mathcal{C}_\lambda$ , it holds from the fact that following derivative is bounded:

$$\left\| \frac{\partial \lambda_t}{\partial \lambda_n^*} \right\| = \left\| \frac{\mu \lambda_t^*}{\|\lambda_t^*\|} \right\| = \mu$$

If  $\lambda_1^* \in \mathcal{C}_\lambda, \lambda_3^* \notin \mathcal{C}_\lambda$ , it can be derived from following inequality:

$$\|\lambda_1 - \lambda_3\| \leq \|\hat{\lambda}_1 - \hat{\lambda}_3\| \leq \zeta \|\hat{\lambda}_1^* - \hat{\lambda}_3^*\| = \zeta \|\lambda_1^* - \lambda_3^*\|$$

where  $\hat{\lambda}$  is the output of  $\Pi_{\mathcal{C}_{\lambda_n, m}}$  from input  $\hat{\lambda}^* = [\lambda_n^*; d\lambda_{t_1}^*; d\lambda_{t_2}^*]$  with large enough  $d$  that satisfies  $\hat{\lambda}^* \notin \mathcal{C}_\lambda$ .

- $\|\lambda_2 - \lambda_3\| \leq \zeta \|\lambda_2^* - \lambda_3^*\|$  for finite constant  $\zeta$

Since  $\lambda_2$  and  $\lambda_3$  share same cross-section  $\mathcal{C}_{\lambda_n, m}$ , the property is directly derived from the contraction property of convex set projection.

Finally, following inequalities hold

$$\|\lambda_1^* - \lambda_3^*\| \leq \|\lambda_1^* - \lambda_2^*\| \quad \|\lambda_2^* - \lambda_3^*\| \leq \|\lambda_1^* - \lambda_2^*\|$$

and therefore Lipschitz continuity is established.  $\blacksquare$

Here, Lipschitz constant is dependent on friction coefficients and increases as friction coefficient get bigger. Based on the lemma, we can derive following theorem.

*Theorem 1:* Suppose that the system is a completely-nodal system. Then VL-FPI in Alg. 1 with the strict operator is contractible for sufficiently small time step  $t$ .

*Proof:* Consider that  $m$ -th contact is S-contact on  $i$ -th node. From

$$\bar{v}_i^{1,l+1} - \bar{v}_i^{2,l+1} = \bar{v}_i^{1,*} - \bar{v}_i^{2,*} + \bar{w}_i R_{c,m}^T (\lambda_{c,m}^1 - \lambda_{c,m}^2)$$

with triangular inequality,

$$\|\bar{v}_i^{1,l+1} - \bar{v}_i^{2,l+1}\| \leq \|\bar{v}_i^{1,*} - \bar{v}_i^{2,*}\| + \bar{w}_i \|\lambda_{c,m}^1 - \lambda_{c,m}^2\|$$

holds. From Lemma 2, let us Lipschitz constant of the strict operator as  $\zeta_m$ . Then

$$\|\lambda_{c,m}^1 - \lambda_{c,m}^2\| \leq \bar{w}_i^{-1} \zeta_m \|\bar{v}_i^{1,*} - \bar{v}_i^{2,*}\|$$

is satisfied and we can find that

$$\|\bar{v}_i^{1,l+1} - \bar{v}_i^{2,l+1}\| \leq (1 + \zeta_m) \|\bar{v}_i^{1,*} - \bar{v}_i^{2,*}\| \quad (35)$$

holds. Now consider that  $m$ -th contact is D-contact on  $i, j$ -th node. Then similarly to above,

$$\begin{aligned} & \|\bar{v}_i^{1,l+1} - \bar{v}_i^{2,l+1}\| \\ & \leq \|\bar{v}_i^{1,*} - \bar{v}_i^{2,*}\| + \zeta_m (\|\bar{v}_i^{1,*} - \bar{v}_i^{2,*}\| + \|\bar{v}_j^{1,*} - \bar{v}_j^{2,*}\|) \\ & \|\bar{v}_j^{1,l+1} - \bar{v}_j^{2,l+1}\| \\ & \leq \|\bar{v}_j^{1,*} - \bar{v}_j^{2,*}\| + \zeta_m (\|\bar{v}_j^{1,*} - \bar{v}_j^{2,*}\| + \|\bar{v}_i^{1,*} - \bar{v}_i^{2,*}\|) \end{aligned}$$

is satisfied and we can find that

$$\begin{aligned} & \|\bar{v}_i^{1,l+1} - \bar{v}_i^{2,l+1}\|^2 + \|\bar{v}_j^{1,l+1} - \bar{v}_j^{2,l+1}\|^2 \\ & \leq \zeta_m' (\|\bar{v}_i^{1,*} - \bar{v}_i^{2,*}\|^2 + \|\bar{v}_j^{1,*} - \bar{v}_j^{2,*}\|^2) \end{aligned} \quad (36)$$

holds for finite  $\zeta_m'$ . Applying (35) and (36) to all contact,

$$\|\hat{v}^{1,l+1} - \hat{v}^{2,l+1}\| \leq \zeta \|\hat{v}^{1,*} - \hat{v}^{2,*}\|$$

is established for finite  $\zeta$ . Therefore from  $\hat{v}^* = (I - WA)\hat{v}^l$ , if  $\|I - WA\| < \frac{1}{\zeta}$ , VL-FPI satisfies contraction property. Now recall the structure of  $A$  in (9). Suppose  $W = \hat{M}^{-1}$  as it satisfies the structure in Prop. 2 as the system is a complete-nodal system. Finally, from

$$\|I - WA\| = \frac{t^2}{2} \|M^{-1}(J_e^T K J_e + E)\|$$

we can reach  $\|I - WA\| < \frac{1}{\zeta}$  by lowering  $t$ .  $\blacksquare$

Although Thm. 1 does not tell about entire convergence of the solver, it provides a partial answer to the uniqueness and existence of the contact NCP solution in the multi-contact situation which is previously unknown. We also believe that this result suggests that in the case of a completely-nodal system, small local deformation of the contact part is possible even when it is a rigid body, so the contradictions arising from assuming an ideal rigid body can be alleviated. Extensive study for generalization of completely-nodal system will be remained as future work. Note that aside from the theoretical analysis, we empirically observe that the solver is robustly convergent in the general case.

## B. Proximal Operator

As mentioned earlier, when the proximal operator is used, it is the same as the solution of a convex optimization, which indicates the existence and uniqueness of the solution. We find that our algorithm can always ensure convergence in this case. To show this, we first utilize following lemma.

*Lemma 3:* Consider the following equations:

$$\begin{aligned} \lambda_{c,m}^1 &= \Pi_{\mathcal{C}_\lambda}(-\gamma_{c,m}^{-1}(\eta_{c,m}^1 + \phi_{c,m})) \\ \lambda_{c,m}^2 &= \Pi_{\mathcal{C}_\lambda}(-\gamma_{c,m}^{-1}(\eta_{c,m}^2 + \phi_{c,m})) \end{aligned}$$

Then for  $\xi_{c,m} = -\gamma_{c,m}^{-1}(\eta_{c,m} + \phi_{c,m}) - \lambda_{c,m}$ , following is holds:

$$(\xi_{c,m}^1 - \xi_{c,m}^2)^T (\lambda_{c,m}^1 - \lambda_{c,m}^2) \geq 0$$

*Proof:* Since  $\mathcal{C}_\lambda$  is a convex set, proximal operator has following property [50]:

$$x = \Pi_{\mathcal{C}_\lambda}(x^*) \rightarrow x^* \in x + \mathcal{N}_{\mathcal{C}_\lambda}(x)$$

where  $\mathcal{N}$  is the normal cone defined as

$$\mathcal{N}_{\mathcal{C}_\lambda}(x) = \{y | y^T(x' - x) \leq 0\} \quad \forall x' \in \mathcal{C}_\lambda, x \in \mathcal{C}_\lambda$$

Therefore,  $\xi_{c,m}^1 \in \mathcal{N}_{\mathcal{C}_\lambda}(\lambda_{c,m}^1), \xi_{c,m}^2 \in \mathcal{N}_{\mathcal{C}_\lambda}(\lambda_{c,m}^2)$  and

$$\begin{aligned} (\xi_{c,m}^1)^T (\lambda_{c,m}^1 - \lambda_{c,m}^2) &\geq 0 \\ (\xi_{c,m}^2)^T (\lambda_{c,m}^2 - \lambda_{c,m}^1) &\geq 0 \end{aligned}$$

is satisfied from the definition of normal cone.  $\blacksquare$

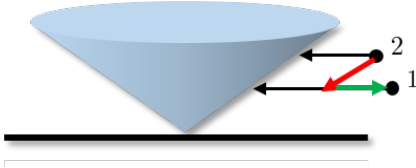


Fig. 5: Counter-example of Lemma 3 on strict operator. Red vector denotes  $\lambda_c^1 - \lambda_c^2$  and green vector denotes  $\xi_c^1 - \xi_c^2$ .

As depicted in Fig. 5, Lemma 3 does not always hold for the strict operator, since it takes ‘two-stage’ projection. Based on this lemma, we can prove the contractibility of our algorithm, which is shown in Thm. 2.

*Theorem 2:* VL-FPI in Alg. 1 with the proximal operator is contractible.

*Proof:* Suppose that  $m$ -th contact is a S-contact on  $i$ -th node. From the

$$\bar{v}_i^{1,l+1} - \bar{v}_i^{2,l+1} = \bar{v}_i^{1,*} - \bar{v}_i^{2,*} + \bar{w}_i R_{c,m}^T (\lambda_{c,m}^1 - \lambda_{c,m}^2)$$

we can derive following equations:

$$\begin{aligned} & \|\bar{v}_i^{1,l+1} - \bar{v}_i^{2,l+1}\|^2 \\ &= \|\bar{v}_i^{1,*} - \bar{v}_i^{2,*}\|^2 + \bar{w}_i^2 \|\lambda_{c,m}^1 - \lambda_{c,m}^2\|^2 \\ &+ 2\bar{w}_i (\bar{v}_i^{1,*} - \bar{v}_i^{2,*})^T R_{c,m}^T (\lambda_{c,m}^1 - \lambda_{c,m}^2) \\ &= \|\bar{v}_i^{1,*} - \bar{v}_i^{2,*}\|^2 - \bar{w}_i^2 \|\lambda_{c,m}^1 - \lambda_{c,m}^2\|^2 \\ &- 2\bar{w}_i (\xi_{c,m}^1 - \xi_{c,m}^2)^T (\lambda_{c,m}^1 - \lambda_{c,m}^2) \end{aligned}$$

Then from Lemma 3, we can find that

$$\|\bar{v}_i^{1,l+1} - \bar{v}_i^{2,l+1}\|^2 \leq \|\bar{v}_i^{1,*} - \bar{v}_i^{2,*}\|^2 \quad (37)$$

holds. Now suppose that  $m$ -th contact is D-contact on  $i, j$ -th nodes and  $\bar{w}_i = \bar{w}_j$  holds. From

$$\begin{aligned} \bar{v}_i^{1,l+1} - \bar{v}_i^{2,l+1} &= (\bar{v}_i^{1,*} - \bar{v}_i^{2,*}) + \bar{w}_i R_{c,m}^T (\lambda_{c,m}^1 - \lambda_{c,m}^2) \\ \bar{v}_j^{1,l+1} - \bar{v}_j^{2,l+1} &= (\bar{v}_j^{1,*} - \bar{v}_j^{2,*}) - \bar{w}_i R_{c,m}^T (\lambda_{c,m}^1 - \lambda_{c,m}^2) \end{aligned}$$

we can derive following equations:

$$\begin{aligned} & \|\bar{v}_i^{1,l+1} - \bar{v}_i^{2,l+1}\|^2 + \|\bar{v}_j^{1,l+1} - \bar{v}_j^{2,l+1}\|^2 \\ &= \|\bar{v}_i^{1,*} - \bar{v}_i^{2,*}\|^2 + \|\bar{v}_j^{1,*} - \bar{v}_j^{2,*}\|^2 \\ &+ 2\bar{w}_i (\lambda_{c,m}^1 - \lambda_{c,m}^2)^T R_{c,m} ((\bar{v}_i^{1,*} - \bar{v}_i^{2,*}) - (\bar{v}_j^{2,*} - \bar{v}_j^{1,*})) \\ &+ 2\bar{w}_i^2 \|\lambda_{c,m}^1 - \lambda_{c,m}^2\|^2 \\ &= \|\bar{v}_i^{1,*} - \bar{v}_i^{2,*}\|^2 + \|\bar{v}_j^{1,*} - \bar{v}_j^{2,*}\|^2 \\ &- 4\bar{w}_i^2 (\lambda_{c,m}^1 - \lambda_{c,m}^2)^T (\xi_{c,m}^1 - \xi_{c,m}^2) - 2\bar{w}_i^2 \|\lambda_{c,m}^1 - \lambda_{c,m}^2\|^2 \end{aligned}$$

Then from Lemma 3, we can find that

$$\begin{aligned} & \|\bar{v}_i^{1,l+1} - \bar{v}_i^{2,l+1}\|^2 + \|\bar{v}_j^{1,l+1} - \bar{v}_j^{2,l+1}\|^2 \\ &\leq \|\bar{v}_i^{1,*} - \bar{v}_i^{2,*}\|^2 + \|\bar{v}_j^{1,*} - \bar{v}_j^{2,*}\|^2 \end{aligned} \quad (38)$$

Applying (37) and (38) to all contacts,

$$\|\hat{v}^{1,l+1} - \hat{v}^{2,l+1}\| \leq \|\hat{v}^{1,*} - \hat{v}^{2,*}\|$$

is established. Therefore, from  $\hat{v}^* = (I - WA)\hat{v}^l$ , contraction property is satisfied if  $\|I - WA\| < 1$  holds. Now consider  $W = \alpha I$  with  $0 < \alpha < 2\sigma_{max}^{-1}(A)$ . It satisfies the structure in Prop. 2 and  $\bar{w}_i = \bar{w}_j$  for D-contact that we suppose. Also,

since  $A$  is a symmetric matrix,  $I - WA = I - \alpha A$  is also a symmetric matrix. Then

$$\|I - WA\| = \rho(I - WA)$$

holds. Also from the positive definite property of  $A$  we can easily find that

$$\rho(I - WA) < 1$$

can be ensured, therefore, the VL-FPI is contractible. ■

The above implies an interesting insight: contacts are contributing property for the contraction property of the iteration process. For this reason, we observe that COND converges faster than proceeding linear solving on a gradient basis in the absence of contact, and convergence is still well established even in the case that  $\|I - WA\|$  is slightly over 1.

### C. Step Size Matrix

As discussed above, choosing  $W$  is the important part of the solver since the sufficient condition to guarantee the global convergence is directly related to the value of  $\|I - WA\|$ . As already known,

$$W = \alpha I \text{ where } \alpha = \frac{2}{\sigma_{min}(A) + \sigma_{max}(A)}$$

can enforces  $\|I - WA\| < 1$  with the property for Prop. 2. However, computing the eigenvalue of a large size matrix is generally time-consuming and using the fixed step size for every iteration and index is not favorable in terms of performance. Therefore, we propose some strategies to determine  $W$  which is simple but efficient. Using the strategies below, convergence problem does not emerged for all the problems we tested.

1) *Frobenius norm minimization:* Frobenius norm of  $I - WA$  which can be written as:

$$\|I - WA\|_F^2 = n - \sum_{i=1}^n w_{ii} a_{ii} + \sum_{i=1}^n \|A_{i*}\|^2$$

where subscript  $i^*$  denotes  $i$ -th row of matrix. Considering  $w_{i_1 i_1} = w_{i_2 i_2} = w_{i_3 i_3} = \bar{w}_i$  for each node that in contact, first-order necessary condition to minimize  $\|I - WA\|_F^2$  can be written as

$$\bar{w}_i = \frac{a_{i_1 i_1} + a_{i_2 i_2} + a_{i_3 i_3}}{\|A_{i_1*}\|^2 + \|A_{i_2*}\|^2 + \|A_{i_3*}\|^2}$$

If the nodes are in D-contact, as described above, 6 components need to be the same value and the result can be derived similarly to above. For the index corresponds to the object that is not in contact, as it does not affect  $\Gamma_c$ ,

$$w_{ii} = \frac{a_{ii}}{\|A_{i*}\|^2}$$

can be used as in [51].

2) *Barzilai-Borwein step size*: Barzilai-Borwein method [52] is the popular method to solve large-scale optimization problem. Even though the problem we are dealing with is not an optimization problem, we find that the strategy can also be well adopted to our framework. Here,  $\alpha$  can be determined by two ways:

$$\alpha_{bb1}^l = \frac{s_l^T s_l}{s_l^T z_l} \quad \alpha_{bb2}^l = \frac{s_l^T z_l}{z_l^T z_l}$$

where  $s_l = \hat{v}^l - \hat{v}^{l-1}$  and  $z_l = A(\hat{v}^l - \hat{v}^{l-1})$ . Any of the two can be selected or can be used alternately as in [52].

We observe that the two methods show similar performance levels and that better methods vary depending on the scenario. Frobenius norm minimization takes longer to construct  $W$  since it corresponds to  $\mathcal{O}(n^2)$  complexity. We find that recycling  $W$  for several time step sections can circumvent this, utilizing the fact that the value of  $W$  does not significantly change for the adjacent time step. Note that reuse of  $W$  does not affect the solver accuracy, since the variables associated with the true physical state (e.g.,  $A, b, J_c$ ) remain unchanged.

## V. RESULTS AND EVALUATION

In this section, simulation results of diverse scenarios using COND with performance evaluation will be presented.

### A. Implementation Details

1) *Tools*: For our implementation, we use Intel Core i5-7500 CPU 3.40GHz (Quad-Core), OpenGL as rendering tool, C++ Eigen as matrix computation library, and C++ OpenMP as parallelization library.

2) *Matrix format*: To handle large-size matrices efficiently, we use compressed sparse column (CSC) format to store  $A$  and  $K$ .  $J_c$  is stored as a stack of  $3 \times 3$  matrices. The matrices which are always guaranteed to be diagonal like  $\Gamma_c$  and  $W$  are stored in vector format.

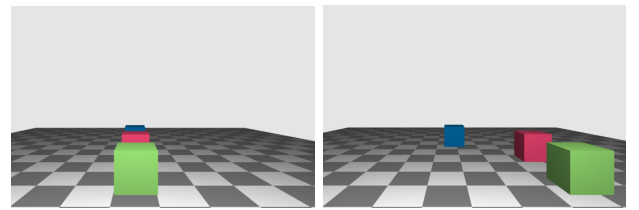
3) *Collision detection*: Collision detection is performed per time step. Here we use self-developed code, which is mainly based on vertex-volume detection.

4) *Solver specification*: For all examples, we use fixed time step as  $t_k = 10$  ms. The strict operator is used in contact solver for all results except in Sec. V-G.

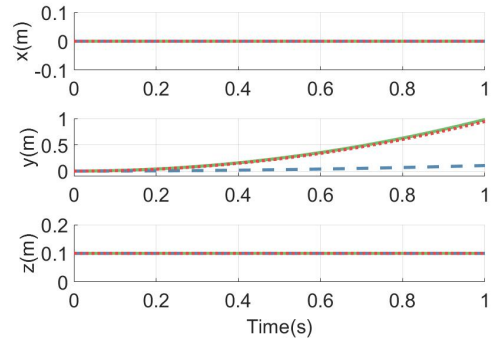
5) *Warm start*: A warm start is utilized to promote the performance of the solver. For the part that is not a virtual node, we directly set  $\hat{v}^1$  as the  $\hat{v}$  value from the previous time step. The warm start of virtual nodes velocity is calculated by multiplying Jacobian mapping  $J_v$  to the original state (i.e., state without virtual nodes) value. Note that warm start is possible because our method is done at velocity-level, while it is difficult in impulse-level iteration methods as contact positions and numbers continue to change.

### B. Box Sliding

We first test a simple scenario of rigid box sliding to verify that VL-FPI in COND converges to the exact contact problem. We place a rigid box of cubes on the floor and give it a constant force in the  $y$ -direction. Since the exact motion of

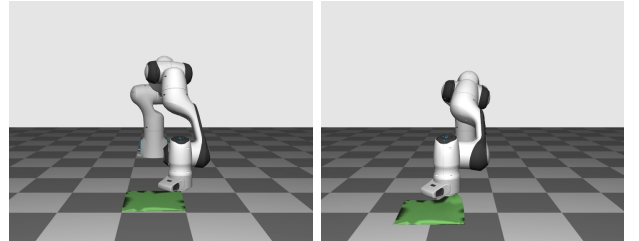


(a) Simulation snapshot (Left: start, Right: after sliding)

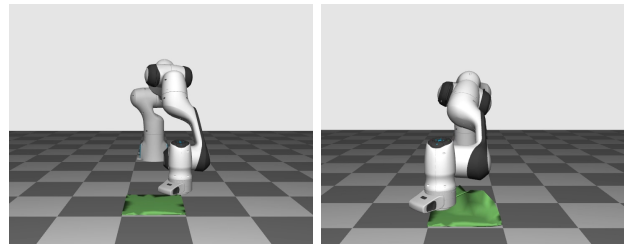


(b) Position plot

Fig. 6: Simulation result for box sliding scenario. Green: analytic solution, Blue: COND with iteration=3, Red: COND with iteration=10.



(a) Soft mat folding manipulation with  $\mu = 0.1$



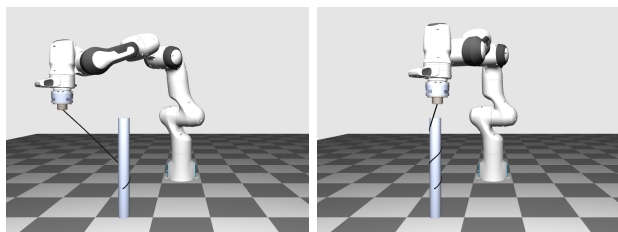
(b) Soft mat folding manipulation with  $\mu = 1.0$

Fig. 7: Soft mat folding manipulation with Franka Emika Panda. Friction coefficient between the floor and the mat is set differently.

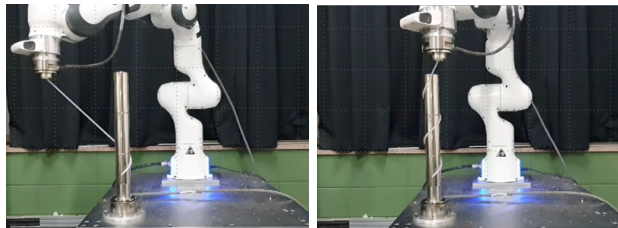
the box is expected analytically in this case, we compare it with our simulation result as in Fig. 6. The result clearly shows that the solver shows the exact solution as iteration increases. For insufficient iteration, we can find the result do not reflect dynamics (external force, in this case) well, yet still comply the contact condition. It also shows that our virtual node based nodal contact formulation works well as contact behavior remains accurate.

### C. Deformable Object Manipulation

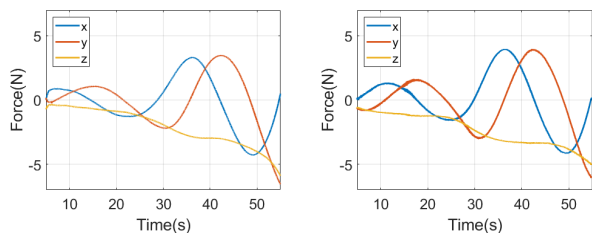
One of the most important scenarios in robotics where rigid and deformable bodies coexist is the manipulation of



(a) Cable winding manipulation simulation



(b) Cable winding manipulation experiment



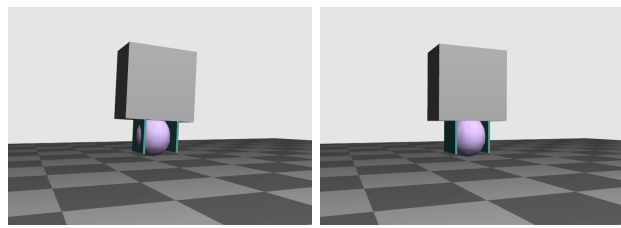
(c) End effector force comparison. Left: simulation, Right: experiment

Fig. 8: Comparison of simulation and experiment for cable winding operation.

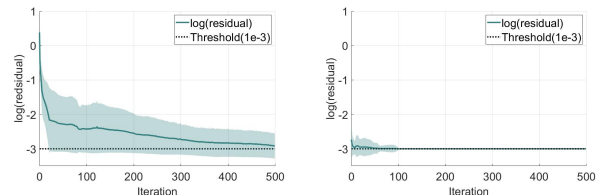
deformable objects using the rigid manipulator, as have been dealt with recently in numerous studies [11], [12], [53]. We test two scenarios - soft mat manipulation and flexible cable manipulation using a torque-controlled robot (Franka Emika Panda). For both scenarios, offline path planning with passivity-based joint tracking control is utilized.

For the soft mat manipulation scenario, to verify whether the simulation is conducted accurately, we compare the results by changing the friction coefficient. For the low friction coefficient ( $\mu = 0.1$ ) case, we find that the mat is first attached to the floor, but eventually slips on the floor as the robot dragged them gradually to fold it (stick-slip transition). Meanwhile, for the high friction coefficient case ( $\mu = 1.0$ ), the mat does not slip on the floor until the robot fully operates. Here, co-rotational FEM model is used to formulate the deformable part dynamics and parameters are set as:  $E = 50$  kPa,  $\nu = 0.3$ . We test on various node and element numbers that are specified in Sec. V-E and confirm that COND shows plausible behavior regardless of how fine the mesh is constructed. The result is illustrated in Fig. 7.

For the flexible cable manipulation scenario, we perform cylinder winding using robot arm and also conduct the experiment to compare with the simulation result. Here, dynamics of flexible cable is constructed using Cosserat rod model [54] and parameters of the cable are measured following to [31]:  $E = 2.954$  MPa,  $\nu = 0.49$ ,  $\mu = 1.3$ . To evaluate the consistency, we measure the force applied to the end effector of



(a) Snapshot of softball gripping manipulation simulation. Left: NCP-PGS solver, Right: COND.



(b) Logarithm of residual value through iteration. Left: NCP-PGS solver, Right: COND.

Fig. 9: Comparison of NCP-PGS solver and COND in softball gripping manipulation simulation.

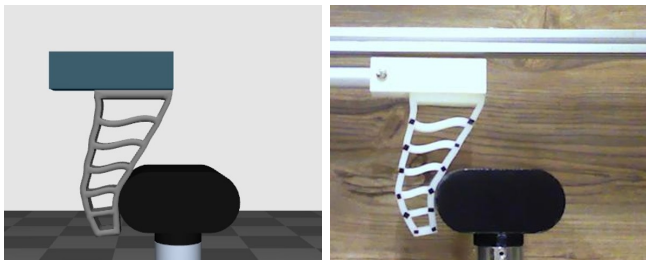
the robot arm during the winding operation task using the F/T sensor (ATI Gamma). As shown in Fig. 8, our simulation result fits well with the experimental force result (RMS norm error: 0.50 N) and also tracks desired pitch well. This shows that our iterative scheme accurately addresses contact conditions while reflecting models that contain material properties.

#### D. Gripping

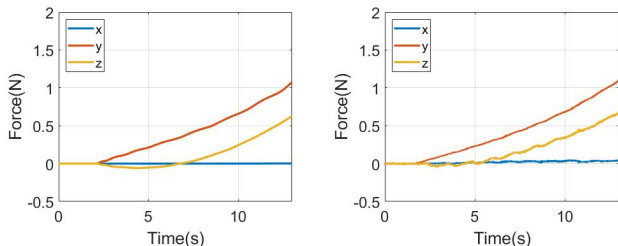
Gripping is also an important challenge in the robotic field, as performing robust gripping tasks in various situations is studied in many places [55], [56]. Unlike the above scenarios, gripping scenarios induce the combined contact situation between both dynamically moving hard and soft parts, which should be handled in a D-contact manner. We perform simulation for the following two cases; rigid gripper grasps soft object and soft gripper grasps a rigid object.

For the rigid gripper-soft object scenario, we design the gripper consists of 6 DOF rigid bodies with 2 DOF prismatic joints which perform grasping of softball. Soft ball is modeled by co-rotational FEM and parameters are set as  $E = 1$  MPa,  $\nu = 0.4$ . Friction coefficient is set to  $\mu = 0.5$ .

We compare the result from COND with projected Gauss-Seidel solver (PGS) [14], which is one of the most widely used methods. Based on standard impulse-based transition (i.e.,  $J_c A^{-1} J_c^T$ ), it performs a projection of each contact while Gauss-Seidel process. Since we used the strict operator, we also use NCP-PGS here. As a result shown in Fig. 9(a), gripping is succeeded in both simulations, which can be considered legitimate due to friction between soft ball and gripper. However, in the result from the PGS-based solver, a big amount of penetration with tilting behavior of the gripper is occurred despite using a large number of max iteration (i.e., 500). This is because the Delassus operator is ill-conditioned as the object is captured symmetrically on both sides, and thus the convergence of the solver is degraded. This is also well shown in Fig. 9(b), as it can be seen that the residual of the



(a) Snapshot of soft gripper manipulation scenario (single gripper). Left: simulation, Right: experiment.



(b) Force plot of soft gripper manipulation scenario. Left: simulation, Right: experiment.

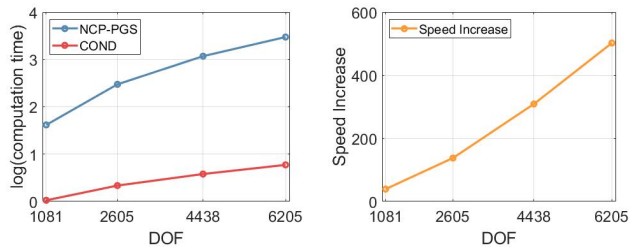
Fig. 10: Comparison of simulation and experiment for soft gripper manipulating scenario.

PGS iteration very slowly converges in contrast to COND. By the way, the residual in the solver converges quickly and does not generate penetration. This implies that COND, despite being very fast, is not significantly affected by the ill-conditioned contact situation.

For the soft gripper-rigid object scenario, we simulate the contact situation with the gripper and the object and compare it with the actual experimental results. The soft part is made of liquid silicone Ecoflex 0050 (Smooth-on Inc.), which is attached to a linear actuator so that it could be operated as a gripper. We attach markers to the grippers so that the displacement can be measured by vision sensor (SC-FD110B). The rigid object part is manufactured using a 3D printer (PLA) and connected to the F/T sensor (ATI Gamma) to measure contact force. We adopt the material parameter of Ecoflex 0050 reported in [57] (Young modulus: 83 kPa, Poisson ratio: 0.42), and the friction coefficient is identified through a simple stick-slip test and a value of 2.1 is obtained. As the results in Fig. 10, the simulation using COND is well matched to experiment both for displacement and force result. (RMS force norm error: 0.09 N, RMS displacement norm error: 1.9 mm). This shows that our method can reliably and accurately solve the dynamics of the soft body, even for D-contact situations with virtual node formulation.

### E. Computation Time

We check the execution time of the solver to validate the efficacy of COND. We use NCP-PGS solver which is described above as a baseline, as it is a fairly universal method [14], [18], [58]. We implement the NCP-PGS using sparse Cholesky factorization in Eigen library. All physical parameters are defined as described in above subsections. Also threshold value for VL-FPI is adjusted between  $10^{-6}$  to  $10^{-3}$



(a) Logarithm of computation time

(b) Speed increase

Fig. 11: Computation time comparison for Franka soft mat scenario with various number of node. Speed increase denotes the ratio of computation time of NCP-PGS solver with respect to computation time of COND. Time unit: ms

according to the scenario, which is found to be capable of producing physically plausible results. The threshold value for global contact solver in NCP-PGS algorithm is fairly determined by considering the norm of  $J_c^T$ .

We divide the whole computation time into two part as 1) dynamics part: a section to construct (1) that includes calculation of constraint error, constraint error Jacobian, mass matrix computation and collision detection, etc. and 2) solver part: a section to obtain  $\hat{v}$  with the contact impulse  $\lambda_c$ . Note that this paper mainly focus on the latter part (i.e., solver time), which is bottleneck of existing solvers. Therefore, the dynamics part may be further accelerated using by various techniques including GPU acceleration [33], fast collision detection [59].

Overall computation time result is organized in Table. I. It is clear that for all scenarios, COND is significant faster compared to the standard solver (NCP-PGS), and the difference grows larger as the size of the system and the number of contacts increase. For the scenario that virtual nodes are not used, dynamics part is calculated in the same way for both NCP-PGS and COND, so the time results for it are averaged together. With virtual nodes, construction of  $A$ ,  $b$ ,  $J_c$  is slightly different, but the overall complexity is nearly identical, so the time required is roughly the same. Also, average iteration number of VL-FPI in COND does not change significantly depending on DOF, most of which come in 30.

To measure scalability more precisely, we check the solver time while changing the node number of the soft body mesh in Franka soft mat scenario. As depicted in Fig. 11, computation time increases as almost linear as DOF increases, which demonstrates the analysis in Sec. III-F. Also, speed increase amount with respect to standard solver grows (super)linearly as DOF increases, which reflects COND has a complexity benefit of more than 1 order compare to NCP-PGS.

### F. Anisotropic Friction

Simulation with anisotropic friction is tested using box slipping scenario. We set ellipsoidal friction model (12) with  $\mu_1 = 0.2$ ,  $\mu_2 = 0.8$  and apply  $y$ -direction force (0.5 N) for first 0.5 s and then apply  $x$ -direction force (0.5 N) for next 0.5 s. In Fig. 12, we can find that the box moves slowly for the first 0.5 seconds, then the movement speeds up after the direction of the force changes.

Scenario	System dim.	Constraint num.	Max. contact	Dynamics time (NCP-PGS)	Solver time (NCP-PGS)	Dynamics time (COND)	Solver time (COND)	Avg. iter. (COND)
Franka mat	1081	5355	165	2.890	<b>41.43</b>	2.890	<b>1.058</b>	15.41
	4438	24606	724	9.622	<b>1173</b>	9.622	<b>3.799</b>	17.57
Franka cable	967	966	130	1.378	<b>16.66</b>	1.378	<b>0.6385</b>	14.68
	1927	1926	249	2.145	<b>74.04</b>	2.145	<b>1.216</b>	18.13
Gripper softball	1664	13488	101	7.085	<b>62.45</b>	7.180	<b>2.952</b>	20.20
	4397	41568	263	18.23	<b>807.2</b>	18.56	<b>6.111</b>	24.84
Soft gripper	1712	8910	8	4.801	<b>6.779</b>	4.783	<b>1.973</b>	24.06
	14681	108744	37	45.18	<b>648.2</b>	44.47	<b>16.86</b>	28.02

TABLE I: Computation time of solver for various scenario. Time and iteration data are per time step, averaged value. Time units: ms.

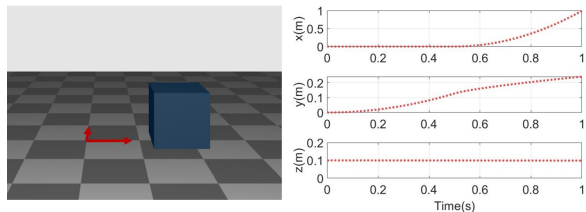
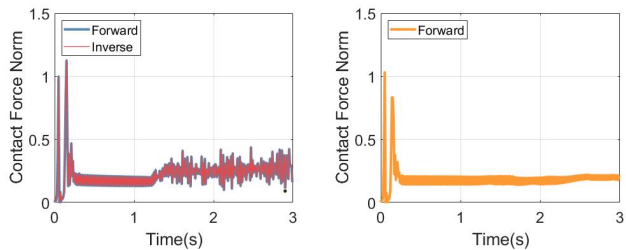
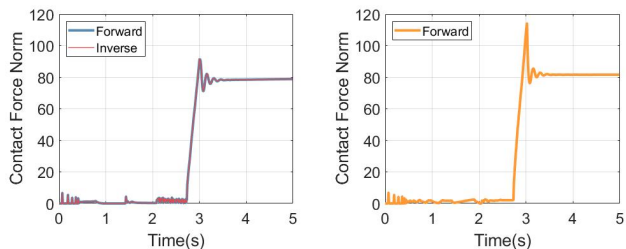


Fig. 12: Box sliding simulation on anisotropic friction region. Left: snapshot, red coordinates visualize anisotropic friction model, Right: position plot.



(a) Norm of contact force applied to the mat during Franka soft mat folding



(b) Norm of contact force applied to the softball during gripping

Fig. 13: Force results from two scenarios. Left: proximal operator, blue line denotes contact impulse norm computed using forward dynamics and red line denotes contact impulse norm computed inversely from the result. Right: strict operator.

### G. Proximal Operator

Performance of COND with the proximal operator is also evaluated. Here, we identify two things - difference in result between strict operator and proximal operator, and whether it has good invertible properties when regularization term is included.

Results are depicted in Fig. 13. We vectorize the forwardly/inversely calculated contact forces applied to all nodes for each time step and take the norm. We can find that invertible property is well preserved as forward result and inverse

Scenario	System dim.	Avg. iter. (w.o. Cheby.)	Avg. iter. (w. Cheby.)
Franka mat	1081	71.48	15.41
Franka cable	967	35.68	14.68
Gripper softball	1664	70.53	20.20
Soft gripper	1712	138.1	24.06

TABLE II: Effect of Chebyshev acceleration in iteration number.

result well matched. This demonstrate the solver successfully handle the convex optimization problem. Regularization term is set as  $\Omega_c = 10^{-3}I$  for both scenarios. In Franka soft mat scenario, the results using proximal operator show that jittering occurs during sliding unlike the results using strict operator. This seems to have occurred due to the fact that Signorini conditions are not exactly satisfied in the proximal operator, and repeatedly take-off and collide simultaneously across nodes. On the other hand, for the softball gripping scenario, the two results are very similar. However, we observe that in the case of the proximal operator, penetration compensation term must be appropriately applied for plausible behavior.

### H. Effect of Chebyshev Acceleration

To evaluate the efficacy of Chebyshev acceleration in COND, we perform simulation in various scenario with and without Chebyshev acceleration and compare the average iteration number for convergence. As shown in Table. II, average iteration number to reach the threshold value is decreased for all scenarios and demonstrates that Chebyshev acceleration effectively works on COND. In the same vein, Nesterov momentum [49] and Anderson acceleration [60] can also be adopted to our framework - implementation and comparison of these will be left for future work.

## VI. CONCLUSION AND FUTURE WORK

In this paper, we propose the new multibody simulation framework (COND) that can resolve the complexity and convergence issue of existing methods. In the framework, velocity-level fixed-point iteration is performed to satisfy dynamics condition while keeping contact condition by solving contact problem with respect to surrogate dynamics at each iteration. Contact nodalization and diagonalization is proposed that make all contact into nodal situations and make the contact solving process of the surrogate dynamics very

fast and simple (i.e., parallelizable and one-shot with no iteration required), while keeping exactness of the contact simulation solution. Theoretical statements related to accuracy and convergence of the solver are presented. Simulations and experiments are conducted and the results demonstrate that our solver is much faster than a standard PGS-based solver as it shows near  $\mathcal{O}(n)$  complexity, while producing results well-matching experimental data. Some possible future work directions are as follows: 1) combination with model order reduction schemes for further improvement of efficiency, 2) efficient differentiation of forward dynamics using our solver which can be utilized in gradient-based optimization methods, 3) strengthened analysis and proofs of convergence and uniqueness of the solution, and 4) development of an open-source framework that can be linked to the reinforcement learning library, as an extension of our project in [https://github.com/INRoL/inrol\\_sim\\_cablewinding](https://github.com/INRoL/inrol_sim_cablewinding).

## REFERENCES

- [1] L. Kunze, N. Hawes, T. Duckett, M. Hanheide, and T. Krajník. Artificial intelligence for long-term robot autonomy: A survey. *Robotics and Automation Letters*, 3(4):4023–4030, 2018.
- [2] Y. Narang, B. Sunarlingam, M. Macklin, A. Mousavian, and D. Fox. Sim-to-real for robotic tactile sensing via physics-based simulation and learned latent projections. In *International Conference of Robotics and Automation*, 2021.
- [3] M. A. Lee, Y. Zhu, P. Zachares, M. Tan, K. Srinivasan, S. Savarese, L. Fei-Fei, A. Garg, and J. Bohg. Making sense of vision and touch: Learning multimodal representations for contact-rich tasks. *Transactions on Robotics*, 36(3):582–596, 2020.
- [4] F. Agostinelli, S. McAleer, A. Shmakov, and P. Baldi. Solving the rubik’s cube with deep reinforcement learning and search. *Nature Machine Intelligence*, 1(8):356–363, 2019.
- [5] Y. Chebotar, A. Handa, V. Makoviychuk, M. Macklin, J. Issac, N. Ratliff, and D. Fox. Closing the sim-to-real loop: Adapting simulation randomization with real world experience. In *International Conference on Robotics and Automation*, 2019.
- [6] J. Hwangbo, J. Lee, A. Dosovitskiy, D. Bellicoso, V. Tsounis, V. Koltun, and M. Hutter. Learning agile and dynamic motor skills for legged robots. *Science Robotics*, 4(26), 2019.
- [7] D. Son, H. Yang, and D. Lee. Sim-to-real transfer of bolting tasks with tight tolerance. In *International Conference on Intelligent Robots and Systems*, 2020.
- [8] L. Pinto, M. Andrychowicz, P. Welinder, W. Zaremba, and P. Abbeel. Asymmetric actor critic for image-based robot learning. In *Robotics: Science and Systems*, 2018.
- [9] E. Valassakis, N. D. Palo, and E. Johns. Coarse-to-fine for sim-to-real: Sub-millimetre precision across the workspace. In *International Conference on Intelligent Robots and Systems*, 2021.
- [10] X. B. Peng, M. Andrychowicz, W. Zaremba, and P. Abbeel. Sim-to-real transfer of robotic control with dynamics randomization. In *International Conference of Robotics and Automation*, 2018.
- [11] J. Matas, S. James, and A. J. Davison. Sim-to-real reinforcement learning for deformable object manipulation. In *Conference on Robot Learning*, 2018.
- [12] H. Zhang, J. Ichnowski, D. Seita, J. Wang, H. Huang, and K. Goldberg. Robots of the lost arc: Self-supervised learning to dynamically manipulate fixed-endpoint cables. In *International Conference of Robotics and Automation*, 2021.
- [13] S. Hofer, K. Bekris, A. Handa, G. C. Gamboa, F. Golemo, M. Mozifian, C. Atkeson, D. Fox, K. Goldberg, Leonard J., C. K. Liu, J. Peters, S. Song, P. Welinder, and M. White. Perspectives on sim2real transfer for robotics: A summary of the r:ss 2020 workshop. In *Workshop in Robotics: Science and Systems*, 2020.
- [14] P. C. Horak and J. C. Trinkle. On the similarities and differences among contact models in robot simulation. *Robotics and Automation Letters*, 4(2):493–499, 2019.
- [15] J. Hwangbo, J. Lee, and M. Hutter. Per-contact iteration method for solving contact dynamics. *Robotics and Automation Letters*, 3(2):895–902, 2018.
- [16] F. Bertails-Descoubes, F. Cadoux, G. Daviet, and V. Acary. A nonsmooth newton solver for capturing exact coulomb friction in fiber assemblies. *Transactions on Graphics*, 30(1):1–14, 2011.
- [17] T. Liu and M.Y. Wang. Computation of three-dimensional rigid-body dynamics with multiple unilateral contacts using time-stepping and gauss-seidel methods. *Transactions on Automation Science and Engineering*, 2(1):19–31, 2005.
- [18] K. Erleben. Rigid body contact problems using proximal operators. In *Eurographics Symposium on Computer Animation*, 2017.
- [19] M. Anitescu and F. A. Potra. Formulating dynamic multi-rigid-body contact problems with friction as solvable linear complementarity problems. *Nonlinear Dynamics*, 14:231–247, 1997.
- [20] J.E. Lloyd. Fast implementation of lemke’s algorithm for rigid body contact simulation. In *International Conference on Robotics and Automation*, 2005.
- [21] M. Anitescu and A. Tasora. An iterative approach for cone complementarity problems for nonsmooth dynamics. *Computational Optimization and Applications*, 47:207–235, 2010.
- [22] E. Todorov. Convex and analytically-invertible dynamics with contacts and constraints: Theory and implementation in mujoco. In *International Conference on Robotics and Automation*, 2014.
- [23] Bullet physics engine. <https://pybullet.org/>.
- [24] Mujoco physics engine. <http://www.mujoco.org/>.
- [25] J. Yoon, I. Hong, and D. Lee. Passive model reduction and switching for fast soft object simulation with intermittent contacts. In *International Conference on Intelligent Robots and Systems*, 2019.
- [26] O. Goury and C. Duriez. Fast, generic, and reliable control and simulation of soft robots using model order reduction. *Transactions on Robotics*, 34(6):1565–1576, 2018.
- [27] Simulation open framework architecture. <https://www.sofa-framework.org/>.
- [28] M. Macklin, M. Müller, and N. Chentanez. Xpbd: Position-based simulation of compliant constrained dynamics. In *International Conference on Motion in Games*, 2016.
- [29] S. Bouaziz, S. Martin, T. Liu, L. Kavan, and M. Pauly. Projective dynamics: Fusing constraint projections for fast simulation. *Transactions on Graphics*, 33(4):1–11, 2014.
- [30] G. Daviet. Simple and scalable frictional contacts for thin nodal objects. *Transactions on Graphics*, 39(4), 2020.
- [31] J. Lee, M. Lee, J. Yoon, and D. Lee. A parallelized iterative algorithm for real-time simulation of long flexible cable manipulation. In *International Conference on Robotics and Automation*, 2021.
- [32] J. Li, G. Daviet, R. Narain, F. Bertails-Descoubes, M. Overby, G. E. Brown, and L. Boissieux. An implicit frictional contact solver for adaptive cloth simulation. *Transactions on Graphics*, 37(4):1–15, 2018.
- [33] M. Macklin, K. Erleben, M. Müller, N. Chentanez, S. Jeschke, and V. Makoviychuk. Non-smooth newton methods for deformable multi-body dynamics. *Transactions on Graphics*, 38(5):1–20, 2019.
- [34] A. R. Champneys and P. L. Varkonyi. The Painleve paradox in contact mechanics. *IMA Journal of Applied Mathematics*, 81(3):538–588, 2016.
- [35] M. Kim, Y. Lee, Y. Lee, and D. J. Lee. Haptic rendering and interactive simulation using passive midpoint integration. *International Journal of Robotics Research*, 36(12):1341–1362, 2017.
- [36] G. F. Moita and M. A. Crisfield. A finite element formulation for 3-d continua using the co-rotational technique. *International Journal of Numerical Method in Engineering*, 39(22):3775–3792, 1996.
- [37] M. Tournier, M. Nesme, B. Gilles, and F. Faure. Stable constrained dynamics. *Transactions on Graphics*, 34(4):1–10, 2015.
- [38] Nicholas J. H. Computing a nearest symmetric positive semidefinite matrix. *Linear Algebra and its Applications*, 103:103–118, 1988.
- [39] P. Volino and N. Magnenat-Thalman. Implicit midpoint integration and adaptive damping for efficient cloth simulation. *Computer Animation and Virtual Worlds*, 16(3-4):163–175, 2005.
- [40] E. R. Johnson and T. D. Murphey. Scalable variational integrators for constrained mechanical systems in generalized coordinates. *Transactions on Robotics*, 25(6):1249–1261, 2009.
- [41] R. Featherstone and D. Orin. Robot dynamics: Equations and algorithms. In *International Conference on Robotics and Automation*, 2000.
- [42] Y. Wang, N. J. Weidner, M. A. Baxter, Y. Hwang, D. M. Kaufman, and S. Sueda. Redmax: Efficient & flexible approach for articulated dynamics. *Transactions on Graphics*, 38(4):1–10, 2019.
- [43] E. Todorov, T. Erez, and Y. Tassa. Mujoco: A physics engine for model-based control. In *International Conference on Intelligent Robots and Systems*, 2012.
- [44] N. Parikh and S. Boyd. Proximal algorithms. *Foundations and Trends in Optimization*, 1(3):127–239, 2014.



- [45] K. Erleben, M. Macklin, S. Andrews, and P. G. Kry. The matchstick model for anisotropic friction cones. *Computer Graphics Forum*, 39(1):450–461, 2020.
- [46] T. Preclik, S. Eibl, and U. Rude. The maximum dissipation principle in rigid-body dynamics with inelastic impacts. *Computational Mechanics*, 62:81–96, 2017.
- [47] H. Wang. A chebyshev semi-iterative approach for accelerating projective and position-based dynamics. *Transactions on Graphics*, 34(6):1–9, 2015.
- [48] S. P. Richard. A simple proof of the banach contraction principle. *Journal of Fixed Point Theory and Applications*, 2:221–223, 2007.
- [49] H. Mazhar, T. Heyn, D. Negrut, and A. Tasora. Using nesterov’s method to accelerate multibody dynamics with friction and contact. *Transactions on Graphics*, 34(3):1–14, 2015.
- [50] C. W. Studer. *Augmented time-stepping integration of non-smooth dynamical systems*. PhD thesis, 2008.
- [51] P. Tarazaga and D. Cuellar. Preconditioners generated by minimizing norms. *Computers & Mathematics with Applications*, 57(8):1305–1312, 2009.
- [52] Y. Dai and R. Fletcher. Projected barzilai-borwein methods for large-scale box-constrained quadratic programming. *Numerische Mathematik*, 100:21–47, 2005.
- [53] P. Zhou, J. Zhu, S. Huo, and D. Navarro-Alarcon. Lasesom: A latent and semantic representation framework for soft object manipulation. *Robotics and Automation Letters*, 6(3):5381–5388, 2021.
- [54] M.B. Rubin. *Cosserat Theories: Shells, Rods and Points*. Springer, 2013.
- [55] N. R. Sinatra, C. B. Teeple, D. M. Vogt, K. K. Parker, Gruber D. F., and R. J. Wood. Ultragente manipulation of delicate structures using a soft robotic gripper. *Science Robotics*, 4, 2019.
- [56] A. Hundt, B. Killeen, N. Greene, H. Wu, H. Kwon, C. Paxton, and G. D. Hager. “good robot!”: Efficient reinforcement learning for multi-step visual tasks with sim to real transfer. *Robotics and Automation Letters*, 5(4):6724–6731, 2020.
- [57] P. Roberts, D. D. Damian, W. Shan, T. Lu, and C. Majidi. Soft-matter capacitive sensor for measuring shear and pressure deformation. In *International Conference on Robotics and Automation*, 2013.
- [58] J. Carius, R. Ranftl, V. Koltun, and M. Hutter. Trajectory optimization with implicit hard contacts. *Robotics and Automation Letters*, 3(4):3316–3323, 2018.
- [59] S. Curtis, R. Tamstorf, and D. Manocha. Fast collision detection for deformable models using representative-triangles. In *Symposium on Interactive 3D Graphics and Games*, 2008.
- [60] J. Zhang, Y. Peng, W. Ouyang, and B. Deng. Accelerating admm for efficient simulation and optimization. *Transactions on Graphics*, 38(6):1–21, 2019.